The Astronomical Journal, 141:99 (16pp), 2011 March doi:10.1088/0004-6256/141/3/99

A MULTICOLOR PHOTOMETRIC STUDY OF THE GALAXY CLUSTER A2589: DYNAMICS, LUMINOSITY FUNCTION, AND STAR FORMATION HISTORY

Shun-Fang Liu[1,2,3], Qi-Rong Yuan[4], Yan-Bin Yang[1,3], Jun Ma[1,3], Zhao-Ji Jiang[1,3], Jiang-Hua Wu[1,3], Zhen-Yu Wu[1,3], Jian-Sheng Chen[1,3], and Xu Zhou[1,3]

[1] National Astronomical Observatories, Chinese Academy of Sciences, Beijing 100012, China; liusf@bac.pku.edu.cn, zhouxu@bao.ac.cn
[2] Graduate University, Chinese Academy of Sciences, Beijing 100039, China
[3] Key Laboratory of Optical Astronomy, National Astronomical Observatories, Chinese Academy of Sciences, Beijing, China
[4] Department of Physics, Nanjing Normal University, Nanjing, China; yuanqirong@njnu.edu.cn
Received 2010 September 8; accepted 2011 January 7; published 2011 February 10

ABSTRACT

Smooth X-ray morphology and non-detection of a radio source at the center of A2589 indicate that it is a typical case of a well-relaxed regular galaxy cluster. In this paper, we present a multicolor photometry for A2589 ($z = 0.0414$) with 15 intermediate bands in the Beijing–Arizona–Taiwan–Connecticut (BATC) system which covers an optical wavelength range from 3000 Å to 10000 Å. The spectral energy distributions (SEDs) for more than 5000 sources are achieved down to $V \sim 20$ mag in about a 1 deg^2 field. A2589 has also been covered by the Sloan Digital Sky Survey (SDSS) in photometric mode only. A cross-identification of the BATC-detected galaxies with the SDSS photometric catalog yields 1199 galaxies brighter than $i = 19.5$ mag, among which 68 member galaxies with known spectroscopic redshifts are found. After combining the SDSS five-band photometric data and the BATC SEDs, photometric redshift is applied to these galaxies to select faint member galaxies. The color–magnitude relation is taken as a further restriction of early-type cluster galaxies. As a result, 106 galaxies are newly selected as member galaxies. Spatial distribution of member galaxies shows a north–south elongation which agrees with the X-ray brightness profile and the orientation of central cD galaxy, NGC 7647. No substructures are detected on the basis of positions and radial velocities of cluster galaxies, indicating that A2589 is a well-relaxed system. The luminosity function of A2589 exhibits a peak at $M_R \sim -20$ mag and a dip at $M_R \sim -19$ mag. The low-density outer regions are the preferred habitat of faint galaxies. With the evolutionary population synthesis model, PEGASE, the environmental effect on the star formation properties for 68 spectroscopically confirmed member galaxies is studied. The outlier faint galaxies tend to have longer timescales of star formation, shorter mean stellar ages, and lower metallicities in the interstellar medium, which can be interpreted in the context of a hierarchical cosmological scenario.

Key words: galaxies: clusters: individual (A2589) – galaxies: distances and redshifts – galaxies: evolution – galaxies: kinematics and dynamics – methods: data analysis

1. INTRODUCTION

As the largest gravitationally bound systems in the universe, galaxy clusters play a central role in cosmological studies, such as studies of the baryon content of the universe, formation of large-scale structure, and the density parameters in cosmological models (Bahcall 1999). For instance, the distribution of cluster velocity dispersions and mass-to-light ratios might provide limits on the amplitude of primordial density fluctuations in hierarchical clustering scenarios (Evrard 1989; Frenk et al. 1990). In the cold dark matter models, galaxy clusters are complex multicomponent systems where galaxies, hot gas, and dark matter evolve in a tightly coupled way (Frenk et al. 1996), and they are driven by accreting these components along filaments (Bekki 2001; Roettiger et al. 1996; Navarro & White 1994; Cen & Ostriker 1994). Therefore, galaxy clusters have been regarded as powerful laboratories for studying the evolution of galaxies in a dense environment where the physical properties of these galaxies might have been influenced by many different mechanisms, including strong galaxy–galaxy interaction (Mihos 2004), harassment (Moore et al. 1998), ram pressure stripping (Quilis et al. 2000), and strangulation (also known as starvation, or suffocation; Bower & Balogh 2004).

According to the hierarchical clustering scenario, galaxy clusters continue to be assembled, and relaxation is not yet complete in most clusters. It is widely appreciated that a regular cluster with no detectable substructure both in spatial distribution and in velocity space is at the most evolved stage. However, significant substructures have been revealed in a large number of rich galaxy clusters through X-ray imaging and optical spectroscopic surveys (Rhee & Latour 1991; Forman & Jones 1982; Beers et al. 1991; Sarazin et al. 1992; Henry & Briel 1993; Burns et al. 1994). Numerical simulation of the evolution of galaxy clusters indicates that at least 50% of apparently relaxed clusters contain significant substructures (Salvador-Sole et al. 1993). Very few clusters with a single central dominant cD galaxy are found to be spherically symmetric in distributions of galaxies and hot gas. Even for the Coma cluster, which was once regarded as an example of a regular and well-relaxed cluster, the projected distributions of galaxies and the X-ray-emitting gas also show convincing evidence of significant substructures on both large and small scales (Colless & Dunn 1996; White et al. 1993; Neumann et al. 2003). Recently, a deep spectroscopic survey for the faint galaxies in the central region of the Coma cluster has confirmed previously identified substructures and identified three new substructures (Adami et al. 2009). Despite a shortage of well-relaxed cD galaxy clusters, for a better understanding of the evolution of galaxies, the clusters at the final evolution stage are worth an extensive investigation with multiwavelength data. In addition, the well-relaxed clusters of galaxies are important laboratories for studying the dark matter in clusters. Because hot gas in the core regions of such clusters

is undisturbed by interactions with the central radio source, it is relatively straightforward to resolve the spatial distribution of the gravitational matter which is dominated by dark matter (Buote & Lewis 2004).

The regular cluster of galaxies A2589 ($z = 0.0414$), located at $23^h24^m00\overset{s}{.}5$, $+16°49'29\overset{''}{.}0$ (J2000.0), with Abell richness $R = 0$ (Abell 1958) and BM type I (Bautz & Morgan 1970), is particularly well suited for such analysis. It appears remarkably relaxed and does not show any obvious signs of ongoing mergers. According to the *ROSAT* images, A2589 is a cluster with a smooth X-ray morphology (Buote & Tsai 1996), and the *ROSAT* PSPC observation reveals a cool gas temperature ($kT \sim 3$ keV) and a high X-ray luminosity ($L_{0.5-2.0\,\mathrm{keV}} \sim 8.5 \times 10^{43}$ erg s^{-1}) for the central region of A2589, defined by a radius of 0.5 Mpc (David et al. 1996). The *Chandra* image with higher spatial resolution shows no substantial morphological disturbance and no cooling flow in the core of A2589 (Buote & Lewis 2004). McCarthy et al. (2004) supposed an entropy injection mechanism to explain the relaxed status of the "non-cooling flow" cluster A2589. Additionally, no bright radio source is detected at the cluster center by the NRAO VLA Sky Survey (NVSS; Bauer et al. 2000).

Previous optical studies of the galaxies in A2589 also show no evidence supporting the presence of subclusters (Beers et al. 1991). It is still a tough task to spectroscopically cover all the dwarf galaxies with low surface brightness (Kambas et al. 2000). As mentioned above, A2589 is not a rich cluster. Abell (1958) appraised its richness as $R = 0$, which means less than 50 member galaxies within the magnitude range m_3 to $m_3 + 2$ (where m_3 is the magnitude of the third brightest galaxy). The multicolor optical photometry therefore becomes an alternative way for picking up faint member galaxies in a cluster. According to their spectral energy distributions (SEDs), the redshifts of galaxies can be estimated using the technique of photometric redshift. The Beijing–Arizona–Taiwan–Connecticut (BATC) photometric survey is designed for such a purpose and allows us to study the properties of member galaxies in nearby ($z < 0.1$) clusters (Yuan et al. 2001, 2003; Yang et al. 2004; Zhang et al. 2010).

The relaxed and structureless appearance of A2589 can be well shown in Figure 1, which presents the smoothed contours of the *ROSAT* All-Sky Survey image in the soft X-ray band (0.1–2.4 keV) and of the NVSS map at 1.4 GHz, superimposed on an optical image of $15' \times 15'$ in the BATC h band. In this paper, we will present a multicolor photometric study of the relaxed cluster A2589, using 15 intermediate filters of the BATC system which covers an optical wavelength region from 3000 to 10000 Å. The paper is organized as follows. In Section 2, we describe the BATC observation and data reduction. The SED selection of faint cluster galaxies is given in Section 3. In Section 4, we will show the main results about spatial distribution, dynamics, luminosity function (LF), and star formation properties of cluster galaxies. Finally, a summary and perspective will be given in Section 5. Throughout this paper we adopt a ΛCDM cosmology model with $H_0 = 70$ km s^{-1} Mpc^{-1}, $\Omega_m = 0.3$, and $\Omega_\Lambda = 0.7$.

2. OBSERVATIONS AND DATA REDUCTION

2.1. BATC Observation

The observations of A2589 were carried out with the BATC filter system which includes 15 intermediate-band filters, namely, $a - k$ and $m - p$, covering the entire optical wavelength range. These intermediate filters are specifically designed to avoid most of the known bright night-sky emission lines (Yan et al. 2000), and they are mounted on the 60/90 cm f/3 Schmidt Telescope at the Xinglong station, National Astronomical Observatories of China. Before 2006 October, the BATC system was equipped with an old 2048 × 2048 Ford CCD camera. The field of view was about 1 deg^2, and the spatial scale was $1\overset{''}{.}7$ per pixel. To pursue a better spatial resolution and a higher sensitivity in blue bands, a new E2V 4096 × 4096 CCD has been put into service. This CCD has a quantum efficiency of 92.2% at 4000 Å and a spatial scale of $1\overset{''}{.}35$ per pixel. The field of view is extended to $92' \times 92'$. The pixel sizes for the old and new CCD cameras are 15 and 12 μm, respectively, corresponding to a pixel size ratio of 5:4. The details of the telescope, camera, and data-acquisition system can be found elsewhere (Zhou et al. 2001; Yan et al. 2000). In order to distinguish explicitly between the Sloan Digital Sky Survey (SDSS) and BATC filter names, in this paper, we refer to the SDSS filters and magnitudes as u', g', r', i', z', with central wavelengths of 3560, 4680, 6180, 7500, and 8870 Å. The transmissions of the BATC and SDSS filters can be found in Yuan et al. (2003).

From 2002 September to 2005 November, only 12 BATC filters, from d to p, were used to target A2589 with the old CCD, discontinuously. Since 2006, the exposures in the a, b, and c bands have been completed with the new CCD camera. In total, we have obtained 169 images with more than 54 hr of exposure, which were selected to be combined. The details of our observation of A2589 are given in Table 1.

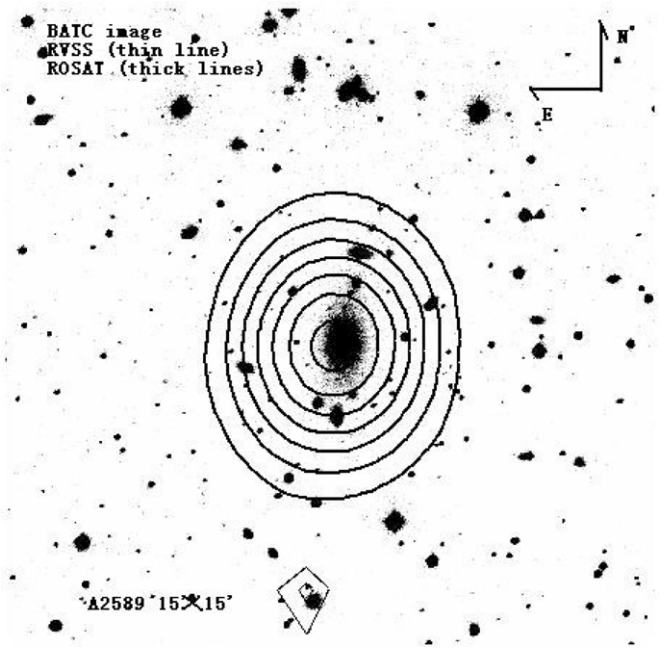

Figure 1. Smoothed contours of the *ROSAT* PSPC image in the soft X-ray band (0.1–2.4 keV, thick line) and of the NVSS map at 1.4 GHz (thin line), superimposed on an optical image of $15' \times 15'$ in the BATC h band. The sizes of Gaussian smoothing windows are adopted as $30''$ and $2'$ for the radio and X-ray contours, respectively.

2.2. Data Reduction

The bias subtraction and dome flat-field correction were done on the CCD images by using *Pipeline I* (Fan et al. 1996; Zhou et al. 2001), the automatic data reduction code for the BATC survey. The cosmic-ray and bad pixel effects were corrected by comparing the images. Before combination, the images were

Table 1
Parameters of the BATC Filters and the Observational Statistics of A2589

No.	Filter Name	λ_c^a (Å)	FWHM (Å)	Exposure (s)	Seeing[b] (arcsec)	Completeness Magnitude	Individual Exposure (s)	Frames
01	*a*	3369.4	277.6	32400	3.99	20.5	1200	27
02	*b*	3921.3	265.5	19200	3.70	20.5	1200	16
03	*c*	4205.6	288.5	13800	3.76	20.5	900	14
							600	2
04	*d*	4528.9	370.6	12000	5.45	21.0	1200	20
05	*e*	4884.7	372.4	13200	5.01	21.0	1200	11
06	*f*	5225.1	333.8	9600	5.08	21.0	1200	8
07	*g*	5793.8	284.5	7200	4.07	20.0	1200	6
08	*h*	6093.6	310.4	6000	4.24	20.0	1200	5
09	*i*	6093.6	310.4	5101	4.41	19.5	1200	4
							301	1
10	*j*	7032.3	163.0	6000	4.38	19.5	1200	5
11	*k*	7539.5	197.2	9000	4.29	19.0	1200	7
							300	2
12	*m*	8012.7	286.6	12000	4.21	19.0	1200	10
13	*n*	8509.5	168.2	11414	4.35	19.0	1200	9
							614	1
14	*o*	9172.9	248.4	18000	3.97	18.5	1200	15
15	*p*	9740.7	272.0	19200	3.85	18.5	1200	16

Notes.
[a] Central wavelengths of the filters.
[b] This column lists the seeing of the combined images.

recentered, and the position calibration was performed by using the Guide Star Catalog (GSC; Jenkner et al. 1990).

To detect sources and measure the source fluxes within a given aperture in the combined BATC images, *Pipeline II*, a photometry package developed on the basis of DAOPHOT (Stetson 1987) kernel (Zhou et al. 2003), was used to perform aperture photometry. The objects with a signal-to-noise ratio greater than the threshold 3.5σ in the *i*, *j*, and *k* bands were detected. Considering the pixel size ratio of 5:4 between the old and new CCDs, we took an aperture radius of 4 pixels (i.e., $r = 1\farcs7 \times 4 = 6\farcs8$) for the images in 12 bands (*d* to *p*), and a radius of 5 pixels (i.e., $r = 1\farcs35 \times 5 = 6\farcs8$) for the images in the *a, b, c* bands. Flux calibration in the BATC system was performed by using four Oke–Gunn standard stars (HD 19445, HD 84937, BD+26 2606, and BD+17 4708; Gunn & Stryker 1983) whose fluxes had been slightly corrected by further BATC observations during photometric nights (Zhou et al. 2001). To check the results of flux calibration via standard stars, we then performed the model calibration on the basis of the stellar SED library (Zhou et al. 1999). The flux measurements derived by these two calibration methods are in accordance with each other for most filters. As a result, the SEDs of 3465 sources were achieved down to $i = 19.5$ within our field of view.

To assess the measurement errors in a specified magnitude, we compared the errors using different subgroups of magnitudes with an interval of 0.5 mag. We found that magnitude error in each filter becomes larger at fainter depth. Errors in the $a - n$ bands were found to be less than 0.02 mag for stars with $i < 16.5$, and more than 0.05 mag for stars with $i > 19.0$.

3. SELECTION OF FAINT MEMBER GALAXIES IN A2589

3.1. Combing the BATC and SDSS SEDs

Owing to low spatial resolution of the BATC images, it is difficult to perfom star–galaxy separation via the surface brightness profiles of detected sources. Alternatively, the color–color diagram is a powerful tool for morphological classification. Fortunately, A2589 has been covered by the SDSS photometric survey, and the star–galaxy classification of all sources down to $r' = 22.0$ has been performed via their light profiles. After cross-identifying these 3465 sources detected by BATC photometry with the SDSS photometric catalog, we obtained a list of 1199 galaxies brighter than $i = 19.5$ within the BATC field of $58' \times 58'$. To check the completeness of the BATC detection of galaxies, we compare the SDSS galaxies down to the same brightness depth (i.e., $r' < 19.5$) in the same region. Within a central region with a radius of $0\fdg5$, there are 555 SDSS-detected galaxies among which 537 galaxies are detected by the BATC, corresponding to a completeness of BATC detection of 96.8%. The spatial scale at cluster redshift $z = 0.0414$ is 0.818 kpc arcsec^{-1}, and the typical seeing of combined images in the BATC bands is about 4.2 arcsec, corresponding to 3.4 kpc, which is smaller than the size of a typical spiral galaxy. Using the photometric catalog of SDSS galaxies, a cross-identification of the 1199 galaxies with $i < 19.5$ was performed to estimate the percentage of object blending due to the seeing effect. A searching circle with a radius of 4.3 arcsec centered at BATC galaxies was adopted, and 27 galaxies were found to have more than one counterpart within the searching circle. The overall blending percentage is about 2.25%. We divided the BATC galaxies into four subsamples with the *i*-band magnitude interval of 1.0 mag, ranging from 15.5 to 19.5; the blending percentages are 2.63%, 4.21%, 2.08%, and 2.03%, respectively.

Furthermore, we made use of the NASA/IPAC Extragalactic Database (NED) to extract available observational information on the bright galaxies on the list. There were 81 galaxies having known spectroscopic redshifts. Note that A2589 has not been covered by the SDSS spectroscopic survey. The available spectroscopic redshifts of galaxies were taken from the relevant literature (Bothun & Schombert 1988; Capelato et al. 1991; Wegner et al. 1999; Smith et al. 2004; Haynes et al. 1997). The majority of spectroscopic redshifts were obtained by Smith

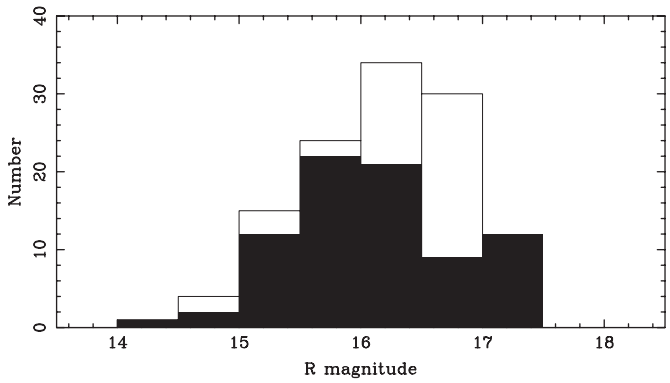

Figure 2. Histograms of the 111 SDSS galaxies selected by the criteria: $R < 17.0$ and $\Delta(B-R) > -0.2$, superposed with the histogram of 81 galaxies with known spectroscopic redshifts (hatched region).

et al. (2004), and their selection criteria for spectroscopy were $R < 17.0$ and $\Delta(B-R) > -0.2$. To estimate the completeness of the spectroscopic sample, we applied the same criteria to the SDSS photometric data. By using the equations in Lupton (2005), the SDSS magnitudes can be transformed into B and R magnitudes. As a result, 111 SDSS galaxies were found to satisfy the criteria. Figure 2 shows the histograms of these 111 SDSS galaxies and 81 galaxies with known spectroscopic redshifts. The overall spectroscopic completeness down to $R = 16.5$ should be about $58/78 \sim 74\%$. Since only 30% of the faint galaxies with $16.5 < R < 17.0$ are spectroscopically covered, the overall completeness down to $R = 17.0$ decreases to $68/108 \sim 63\%$.

For a given galaxy detected by the SDSS imaging observation, two models were used to fit the observed surface brightness profile: (1) the de Vaucouleurs model and (2) the exponential model. To measure the unbiased colors of galaxies, we used the dereddened SDSS model magnitudes which were measured by their flux through equivalent apertures in all SDSS bands. The model (exponential or de Vaucouleurs) of higher likelihood in the r filter was chosen and then applied (i.e., allowing only the amplitude to vary) in the other SDSS bands after convolving with the appropriate point-spread function in each band. Because the resulting model magnitudes were calculated using the best-fit parameters in the r' band, the light was measured consistently through the same aperture in all SDSS bands.

Figure 3(a) shows the relative SDSS and BATC SEDs of the central cD galaxy in A2589, NGC 7647. It is clear that there is a systematic offset between two SEDs, which is called the zero point. A method of interpolation is applied to derive the zero point. Due to a larger magnitude error in the u' band, the magnitude offsets for the other four SDSS filters were calculated by the interpolation algorithm on the basis of the BATC magnitudes in the neighboring bands, and then the average of the second and third largest offsets were taken as the SED zero point. Figure 3(b) gives the combined SED of NGC 7647 after zero-point correction. The zero-point distribution for all the galaxies is presented in Figure 4. It can be seen that the peak of the zero point is -0.2 mag, indicating that the aperture of $r = 6\farcs8$ is large enough to hold the majority of galaxies and to make a different seeing effect negligible. For the most extended central cD galaxy, NGC 7647, our aperture just covers its core region, which leads to a large zero point of nearly 2.0 mag. After zero-point correction, the combined 20 band SEDs for 2101 galaxies detected by BATC and SDSS photometry were achieved.

3.2. Sample of Spectroscopically Confirmed Member Galaxies

Figure 5 shows the distribution of spectroscopic redshifts for 81 galaxies, with a bin size of 0.001. The bulk of the spectroscopic redshifts is concentrated between 0.03 and 0.06, corresponding to A2589. In order to eliminate the background galaxies, we converted the spectroscopic redshifts (z_{sp}) for the galaxies with $0.03 < z_{sp} < 0.06$ into rest-frame velocities (V) by $V = c(z_{sp} - \bar{z}_c)/(1 + \bar{z}_c)$, where c is the speed of light and $\bar{z}_c$ is the cluster redshift with respect to the cosmic background radiation. We used the NED-given cluster redshift of $\bar{z}_c = 0.0414$ for A2589 (Struble & Rood 1999). A Gaussian fit was then applied to the distribution of rest-frame velocities, and a dispersion of $\sigma = 751$ km s^{-1} was derived. With the prevalent selection criterion of 3σ clipping, 68 galaxies with -2215 km s^{-1} $< V <$ 2293 km s^{-1}, corresponding to the z_{sp} range from 0.034 to 0.048, were selected as member galaxies, which we refer to as "sample I." Table 2 lists the SDSS-given celestial coordinates in degrees and the spectroscopic redshift

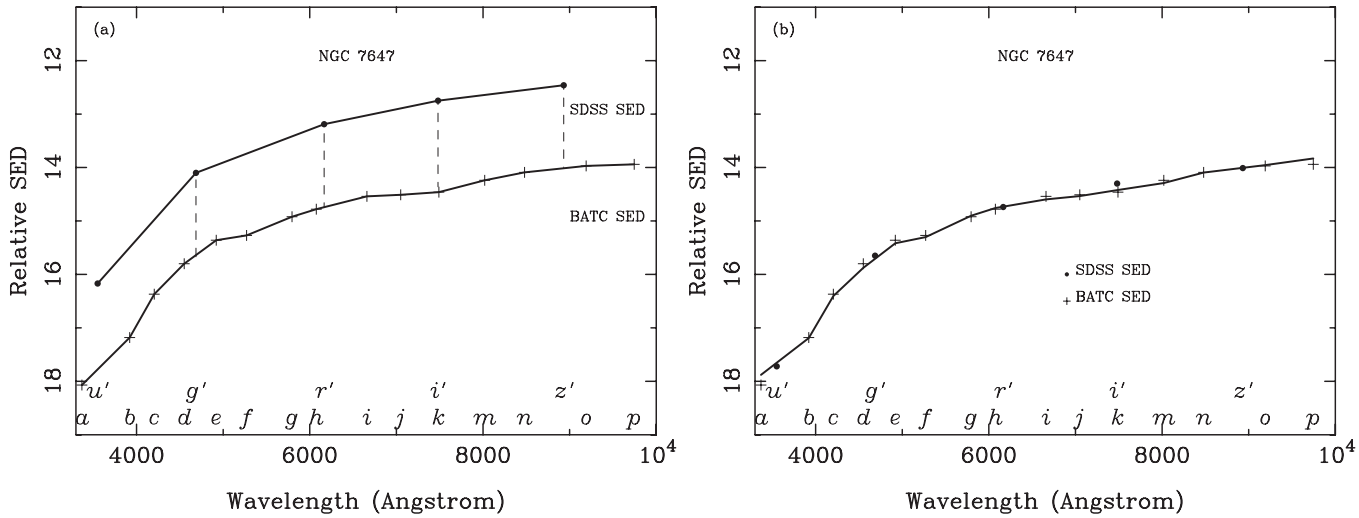

Figure 3. Relative SEDs in the BATC and SDSS systems for the central cD galaxy, NGC 7647, in A2589. (a) Before the zero-point correction (SED connections are denoted by solid lines, and zero points in the g', r', i', z' bands are denoted by dashed lines). (b) After the zero-point correction (the solid line represents the best-fit model SED).

Table 2
Catalog of 68 Spectroscopically Confirmed Member Galaxies in A2589

No.	R.A.	Decl.	z_{sp}	Ref.	No.	R.A.	Decl.	z_{sp}	Ref.
1	350.62835693	16.51060104	0.037286	(4)	35	350.99468994	16.79987144	0.040638	(1)
2	350.64688110	16.70728493	0.040188	(4)	36	350.99569702	16.87491226	0.044764	(3)
3	350.65444946	16.48854637	0.037256	(4)	37	350.99636841	16.81119919	0.042606	(3)
4	350.65954590	17.08135414	0.039137	(4)	38	350.99871826	16.87028122	0.040695	(4)
5	350.72991943	17.12408638	0.039671	(4)	39	351.00134277	16.82041550	0.034737	(1)
6	350.74523926	16.82660675	0.041102	(4)	40	351.00775146	16.81094170	0.035578	(4)
7	350.76705933	16.88853836	0.039070	(4)	41	351.01373291	16.77923775	0.041235	(1)
8	350.79455566	16.91345406	0.041068	(3)	42	351.02078247	16.87013626	0.041295	(3)
9	350.79602051	16.43208885	0.044357	(4)	43	351.02178955	16.66199303	0.040985	(4)
10	350.83938599	16.94395256	0.043143	(4)	44	351.02416992	16.79190254	0.041689	(4)
11	350.85235596	17.02542877	0.039898	(4)	45	351.02755737	16.54348183	0.040064	(4)
12	350.87240601	16.86256027	0.043313	(4)	46	351.03936768	17.11158180	0.039734	(4)
13	350.87268066	16.38849258	0.043523	(4)	47	351.03942871	16.66924858	0.044077	(4)
14	350.88140869	17.15295792	0.043557	(4)	48	351.04479980	16.53371620	0.039234	(4)
15	350.88894653	16.66280174	0.039150	(2)	49	351.05325317	17.10195732	0.044361	(4)
16	350.90270996	16.43026352	0.039961	(4)	50	351.06170654	16.73438454	0.037609	(4)
17	350.90341187	16.56361008	0.044487	(4)	51	351.06555176	16.78513336	0.041382	(2)
18	350.92968750	16.81964874	0.038477	(4)	52	351.07147217	16.92798424	0.041732	(4)
19	350.94128418	16.64007378	0.040208	(4)	53	351.08148193	16.73162270	0.044461	(3)
20	350.94842529	16.85229111	0.041812	(3)	54	351.08395386	16.55175018	0.043470	(4)
21	350.94931030	16.75221825	0.035171	(3)	55	351.09353638	17.04872704	0.041415	(4)
22	350.95083618	16.76874352	0.047183	(4)	56	351.09497070	17.19940758	0.042426	(4)
23	350.95123291	16.70607948	0.042019	(4)	57	351.09564209	16.80035019	0.042386	(4)
24	350.96112061	16.69865799	0.039157	(4)	58	351.13067627	16.86814690	0.035628	(5)
25	350.96188354	16.89692116	0.040441	(4)	59	351.13531494	17.10596466	0.040848	(4)
26	350.96264648	16.52305412	0.042426	(4)	60	351.14495850	16.68141174	0.040405	(3)
27	350.96414185	16.64476776	0.034701	(3)	61	351.17916870	17.13553810	0.041292	(4)
28	350.96905518	16.87223816	0.042670	(2)	62	351.19665527	16.94142342	0.043236	(4)
29	350.97305298	16.88004684	0.044984	(4)	63	351.24346924	16.53924561	0.042186	(4)
30	350.97683716	16.68067169	0.045195	(3)	64	351.30581665	16.40709877	0.039030	(4)
31	350.98266602	16.91675758	0.041212	(4)	65	351.30831909	16.82109833	0.043984	(4)
32	350.98645020	16.75003433	0.038326	(4)	66	351.33325195	17.02133942	0.041022	(4)
33	350.98931885	16.77722740	0.041118	(3)	67	351.33901978	16.68581009	0.041722	(4)
34	350.99304199	16.75839233	0.041949	(4)	68	351.39672852	16.54359245	0.041722	(4)

References. (1) Bothun & Schombert 1988; (2) Capelato et al. 1991; (3) Wegner et al. 1999; (4) Smith et al. 2004; (5) Haynes et al. 1997.

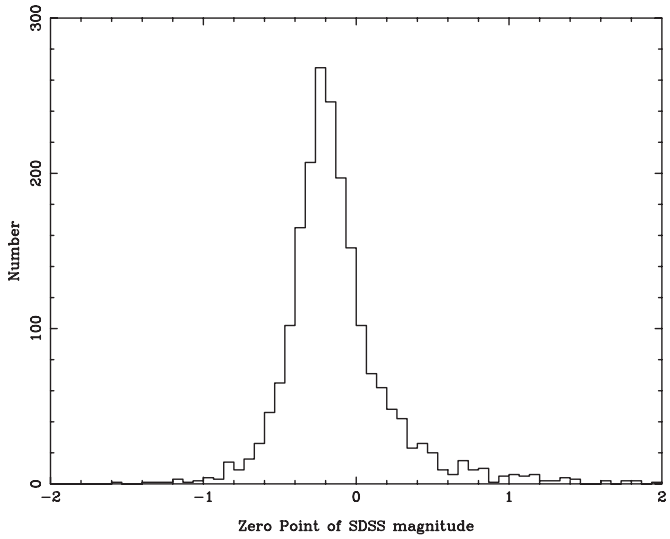

Figure 4. Distribution of the zero points for the galaxies brighter than $i = 19.5$ detected by both multicolor surveys.

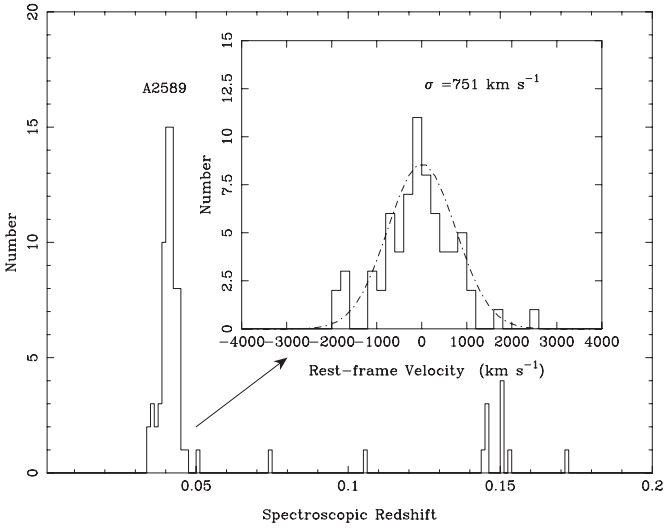

Figure 5. Distribution of spectroscopic redshifts for 81 galaxies detected by both multicolor surveys. The embedded panel shows the histogram of rest-frame velocities for 68 member galaxies.

in the literature for these 68 member galaxies in sample I, in order of right ascension. The embedded panel of Figure 5 shows the histogram of rest-frame velocities for sample I with a Gaussian fit.

With only 26 member galaxies in cluster A2589, Capelato et al. (1991) derived a Gaussian velocity distribution with $\mu_{cz} = 12437 \pm 91$ km s^{-1} and $\sigma = 415^{+119}_{-58}$ km s^{-1}. Based

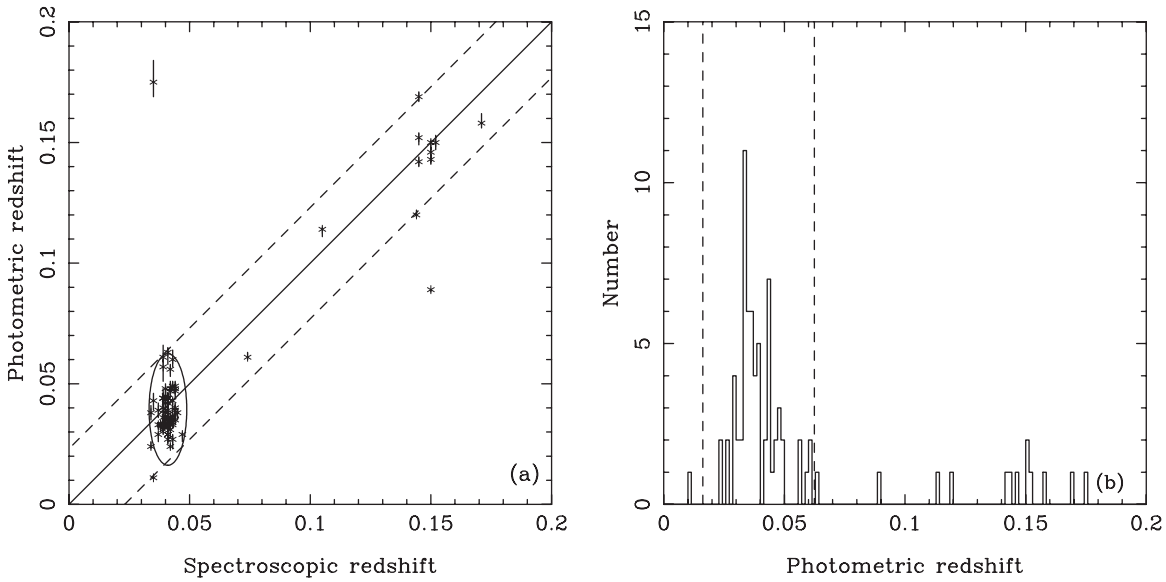

Figure 6. Left: comparison between photometric redshift (z_{ph}) and spectroscopic redshift (z_{sp}) for 81 galaxies with known spectroscopic redshifts in the region of A2589. Right: the distribution of photometric redshifts of 81 known spectroscopic redshift galaxies. The dashed lines are the 3σ range of the photometric redshift.

on 30 member galaxies, Beers et al. (1991) characterized the distribution of measured galaxy velocities by using the ROSTAT software. Two resistant and robust estimators (namely, the biweight location C_{BI} and scale S_{BI}), analogous to the velocity mean and standard deviation, were defined to characterize the velocity distribution (Beers et al. 1990). Beers et al. (1991) found $C_{BI} = 12475^{+199}_{-139}$ km s^{-1} and $S_{BI} = 624^{+457}_{-274}$km s^{-1}. For 68 spectroscopically confirmed member galaxies, we used the ROSTAT software to calculate the biweight location and scale and achieve $C_{BI} = 12122 \pm 90$ km s^{-1} and $S_{BI} = 737 \pm 85$ km s^{-1}. Comparatively, the biweight location in our statistics is smaller, and the biweight scale is larger with smaller uncertainties. In addition, the ROSTAT statistics for the velocity distribution show that the number of large gaps is 0, which means that A2589 might be a virialized system.

3.3. Photometric Redshift Technique

It is well known that the technique of photometric redshift can be used to estimate the redshifts of galaxies on the basis of the SED information given by multicolor photometric surveys. With the development of large and deep field surveys, this technique has been widely applied (Lanzetta et al. 1996; Arnouts et al. 1999; Furusawa et al. 2000). Based on the standard SED-fitting code HYPERZ (Bolzonella et al. 2000), procedures for estimating photometric redshifts have been developed especially for the BATC multicolor photometric system (Yuan et al. 2001; Xia et al. 2002). For a given object, the photometric redshift, z_{ph}, corresponds to the best fit (in the χ^2 sense) between its photometric SED and the template SED. The SED templates for normal galaxies are generated by convolving the galaxy spectra in the template library with the transmission curves of the BATC and SDSS filters. In our SED fitting, we used the templates of normal galaxies in the GISSEL98 (Galaxy Isochore Synthesis Spectral Evolution Library; Bruzual & Charlot 1993). A dust extinction with a reddening law of the Milky Way (Allen 1976) was adopted, and the A_V was flexible in a range from 0.0 to 0.5, in steps of 0.05. As a test, we first let the photometric redshift vary in a wide range from 0.0 to 1.0, with a step of 0.01, and only five galaxies were found to have $z_{ph} > 0.5$. Then we searched the z_{ph} values for 1199 galaxies brighter than $i = 19.5$ in a range from 0.0 to 0.5, with a smaller step of 0.005.

When running HYPERZ, we developed an iterative method to discard the bad magnitudes in the observed SED. For a given galaxy, the first run of HYPERZ gives the best-fit template SED and the observed magnitude at a specified filter with maximum deviation from the best-fit SED is selected. If its maximum deviation exceeds five times the magnitude error, we will discard this magnitude in the observed SED and search for the best SED fitting again. In the worst case scenario, three magnitudes in an observed SED are allowed to be discarded in order to obtain a more accurate photometric redshift.

As a result, we obtained the photometric redshifts for 1199 galaxies brighter than $i = 19.5$, including the 81 galaxies with known z_{sp} values. Figure 6(a) shows the redshift comparison of these 81 galaxies. It is obvious that our z_{ph} estimate is basically consistent with the z_{sp} values. For the 68 member galaxies, the mean photometric redshift is 0.0393, and the standard deviation is 0.0077. The solid line denotes $z_{ph} = z_{sp}$, the dashed lines indicate $\pm 3\sigma$ deviations (i.e., $3 \times 0.0077 = 0.023$) in the z_{ph} estimate, and the error bar of z_{ph} corresponds to the 68% confidence level in our z_{ph} determination. Considering the selection algorithm of 3σ clipping in the z_{ph} space, 66 (about 97%) of 68 member galaxies have z_{ph} values between 0.016 and 0.062 (i.e., $\bar{z}_{ph} \pm 3\sigma$); only two spectroscopically confirmed member galaxies are left out. This z_{ph} range (shown in Figure 6(b) with the dashed lines) is taken as a criterion for selecting the member candidates from the remaining 1118 ($= 1199 - 81$) galaxies without z_{sp} values. Figure 7(a) shows the average $|z_{ph} - z_{sp}|$ as a function of the BATC i-band magnitude. The four magnitude bins are defined as $i < 15.5$, $15.5 < i < 16.0$, $16.0 < i < 16.5$, and $i > 16.5$. The standard errors of $|z_{ph} - z_{sp}|$ are 0.0066, 0.0041, 0.0027, and 0.0135, respectively. A similar statistic for z_{ph} uncertainties for 1199 galaxies is given in Figure 7(b), indicating that the z_{ph} uncertainty given by the SED-fitting code HYPERZ also depends on the magnitude. The four magnitude bins are defined as $15.5 < i < 16.5$, $16.5 < i < 17.5$, $17.5 < i < 18.5$, and $18.5 < i < 19.5$ and their standard errors are 0.0011, 0.0018, 0.0037, and 0.0104, respectively. For the faint galaxies with greater magnitude

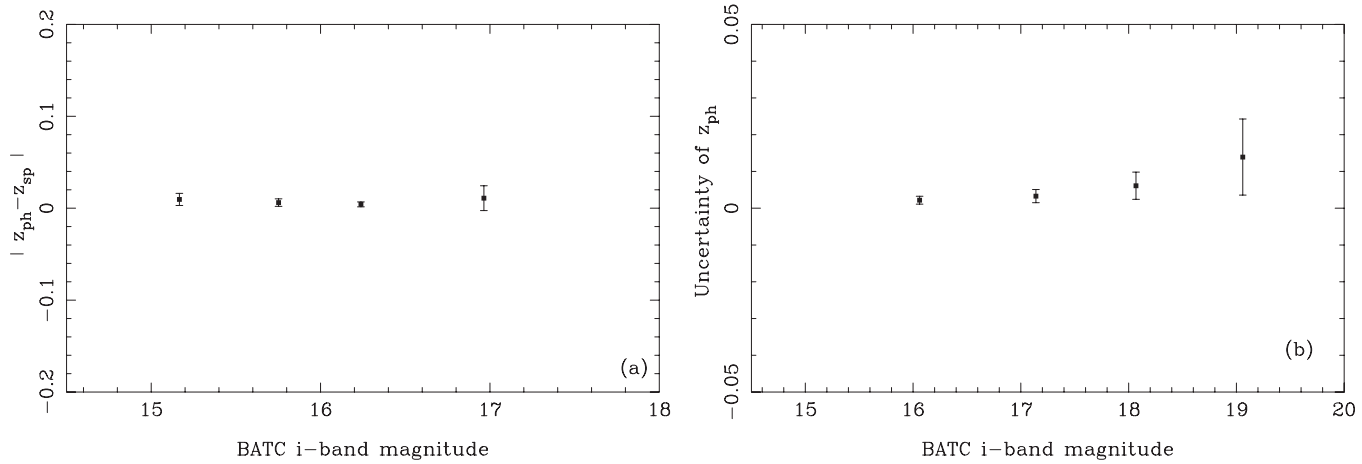

Figure 7. Left: plot of the average deviations, $|z_{ph} - z_{sp}|$, and standard errors (denoted by error bars) as a function of BATC *i*-band magnitude. The four magnitude bins are defined as i <15.5, 15.5 < i < 16.0, 16.0 < i < 16.5, and i >16.5. The standard errors of $|z_{ph} - z_{sp}|$ are 0.0066, 0.0041, 0.0027, and 0.0135, respectively. Right: plot of the uncertainty of 1199 photometric redshits as a function of BATC *i*-band magnitude. The four magnitude bins are defined as 15.5 < i < 16.5, 16.5 < i < 17.5, 17.5 < i < 18.5, and 18.5 < i < 19.5, and their standard errors are 0.0011, 0.0018, 0.0037, and 0.0104, respectively.

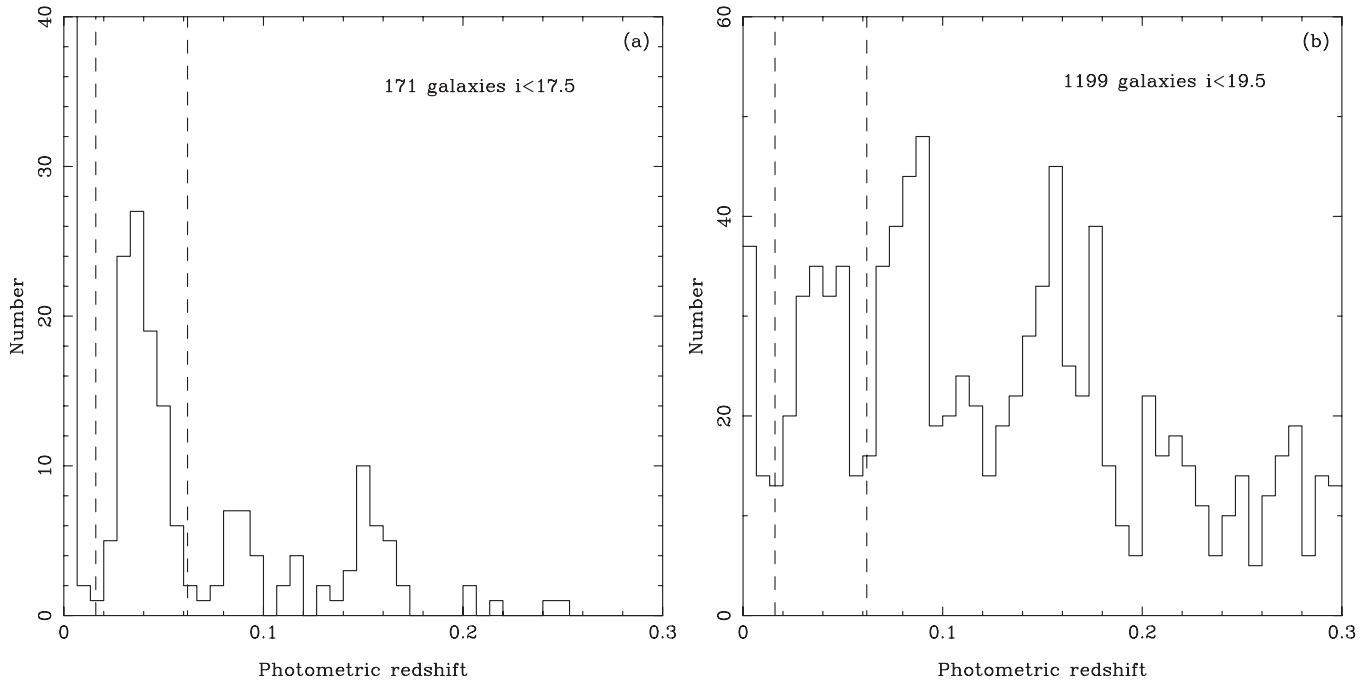

Figure 8. Distributions of estimated photometric redshifts for (a) 171 galaxies brighter than $i = 17.5$ and (b) 1199 galaxies brighter than $i = 19.5$.

errors, the degree of SED fitting tends to be worse, which results in larger uncertainties.

After applying the z_{ph} technique to the combined SEDs of 1118 galaxies, 110 faint galaxies (including 73 early-type galaxies and 37 late-type galaxies) were identified as member galaxy candidates of A2589. Figure 8 shows the z_{ph} histograms for the galaxies in different detection depths. Panel (a) gives the z_{ph} distribution for the 171 bright galaxies with $i < 17.5$, and panel (b) gives the same for the 1199 galaxies with $i < 19.5$. The dashed lines denote the photometric redshift range of cluster member candidates. At the detection depth of $i = 17.5$, corresponding to the limit of the SDSS spectroscopy, the peak at $z_{ph} = 0.04$ (contributed by cluster A2589) is very prominent. As the magnitude limit approches the faint end, the peak of A2589 is still remarkable although a large number of background galaxies are detected, which demonstrates the reliability of our method of combining the BATC and SDSS photometric data and the SED-fitting procedure.

3.4. The Color–Magnitude Correlation

A correlation between the color and absolute magnitude of early-type galaxies, the so-called CM relation, has been found for many rich galaxy clusters (see Bower et al. 1992, and references therein). For early-type galaxies in a cluster, the brighter galaxies tend to have colors that are redder than those of the fainter galaxies. This relation can be used to verify the membership selection of the early-type galaxies within the BATC field (Yuan et al. 2001). In order to select the early-type member galaxies, we use the Hubble types of the best-fit SED templates as morphology classifications. Figure 9 presents the correlation between the color index $u' - p$ versus h magnitude for the known and new early-type member candidates. The

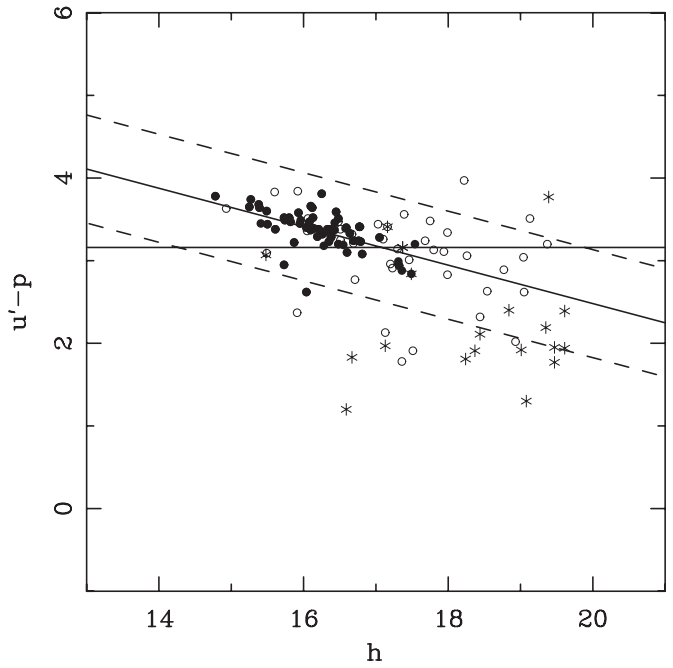

Figure 9. Color–magnitude relation for 130 early-type galaxies in A2589, including 65 early-type galaxies with known spectroscopic redshifts (filled circles) and 65 newly selected member candidates (open circles). The 44 late-type member galaxies are also plotted (stars). A linear fit is given to the 65 spectroscopically confirmed early-type members, and the dashed lines correspond to the $\pm 1\sigma$ of the linear fitting.

open circles denote newly selected early types and the filled circles denote the known early types. The solid line denotes the least-squares fit for the linear relation with 65 known early-type galaxies: $u' - p = -0.26(\pm 0.04)h + 7.53(\pm 0.70)$. The dashed lines represent $\pm 1\sigma$ deviation. Taking all photometric early types into account, a horizontal line, $u' - p = 3.15$, seems to also be a good model of the red sequence, which means red galaxies in A2589 might have a typical $u' - p$ color. Note that the positive CM relation might be artificial because red galaxies are likely to be classified as early types by the HYPERZ code.

As shown in Figure 9, most of the early-type candidates agree with the CM correlation derived from the known early-type galaxies. There are eight early-type candidates with colors beyond the 2σ deviation of intercept that have probably been misclassified. Using only the templates of late-type galaxies, we again apply the SED-fitting procedures to these eight candidates. As a result, four of them are found to have the best-fit template SEDs of Sa galaxies with redshifts between 0.016 and 0.062, and they are therefore regarded as late-type member galaxies. The remaining four candidates are excluded from the list of member galaxies.

Finally, we obtain a list of 106 ($= 110 - 4$) newly selected member galaxies. Combined with the 68 spectroscopically confirmed member galaxies, we have obtained an enlarged sample of 174 member galaxies which includes 130 early-type galaxies and 44 late-type galaxies. We refer to this sample as "sample II" hereafter. Table 3 presents the catalog of SED information for the 106 newly selected members, including the ID number, the SDSS-given celestial coordinate in degrees, photometric redshift, morphological class of the best-fit template, and combined SED information. The classification indices in a range from 1 to 7 are defined to denote E, S0, Sa, Sb, Sc, Sd, and Im galaxies, respectively. A magnitude of 99.00 indicates non-detection in the specified band.

4. PHYSICAL PROPERTIES OF REGULAR CLUSTER A2589

4.1. Spatial Distribution

The X-ray images obtained in the *ROSAT* (Buote & Tsai 1996) and *Chandra* (Buote & Lewis 2004) observations support a picture that A2589 has a smooth X-ray morphology and no sign of ongoing merger. The optical map of cluster galaxies also shows no evidence of subclusters in A2589 (Beers et al. 1991). The projected distribution of the 68 member galaxies in sample I is given in Figure 10(a). In order to show the overall morphology of a two-dimensional distribution of galaxies, we superpose the contour map of the surface density that has been smoothed by a Gaussian window with $\sigma = 3'$. It is easy to find that A2589 concentration is rather compact: more than 50% of bright known member galaxies are located within a small circular region with $r = 0.5$ Mpc. The contour profiles tend to be more asymmetric at larger radius, but no detached clumps (i.e., substructures) of galaxies are detected. Figure 10(a) shows an elongation along the north–south direction, which seems to agree with the X-ray brightness profile and the orientation of central cD galaxy.

For the 174 member galaxies in sample II, the projected distribution is also given in Figure 10(b). We superpose the contour map of the spatial distribution that has been smoothed by a Gaussian window with $\sigma = 4'$. The filled circles denote the 68 member galaxies with known spectroscopic redshifts, and the open circles denote the 103 newly selected member galaxies. Though the sample size increases by nearly 150%, the profile of surface density does not change a lot, with the same orientation and shape in the central region, and no discrete substructure is detectable at a low surface density level of 0.14 arcmin^{-2}.

4.2. Localized Velocity Structure

The projected distribution of galaxies appears smooth and relaxed, which might be due to projection effect. A true substructure should be verified in the line-of-sight velocity space. The κ-test has been commonly used for this purpose, which was developed by Colless & Dunn (1996) for quantifying localized variation in velocity distribution. A test statistic κ_n is defined to characterize the local deviation on the scale of the groups of n nearest neighbors based on the Kolmogorov–Smirnov test (K-S test). A larger value of κ_n means a greater possibility that the local velocity distribution differs from the whole distribution. The probability that κ_n is larger than the observed value, $P(\kappa_n > \kappa_n^{\rm obs})$, can be estimated by Monte Carlo simulations by randomly shuffling velocities. Table 4 gives the results of the κ-test for samples I and II, and 10^3 simulations are made for all cases. A limit of $P(\kappa_n > \kappa_n^{\rm obs})$ for substructure detection is 5%, corresponding to the 2σ significance. For the 68 member galaxies in sample I, the probability $P(\kappa_n > \kappa_n^{\rm obs})$ is found to be about 80% (much more than the limit of 5%) in a wide range of neighbor size, which strongly supports non-detection of substructure. Even for the enlarged sample of 174 member galaxies, the probability $P(\kappa_n > \kappa_n^{\rm obs})$ is still over 16%, which is two times greater than the limit of 5%. No substructures are detected at more than 2σ significance on the basis of sample II.

Figure 11 shows the bubble plots of the localized velocity variation, using the neighbor size $n = 9$ for both samples. The bubble size for each galaxy is proportional to $-\log[P_{\rm K\text{-}S}(D > D_{\rm obs})]$. Therefore, larger bubbles indicate a greater difference between local and overall velocity distributions. There is no prominent bubble clustering in the core region of A2589. For the 68 spectroscopic galaxies in sample I, the central bubbles are very tiny,

Table 3
Catalog of 106 Newly Selected Candidates of Member Galaxies in A2589

No.	R.A.	Decl.	z_{ph}	T	a	b	c	d	e	f	g	h	i	j	k	m	n	o	p	u'	g'	r'	i'	z'
1	350.52581787	16.92402267	0.048	1	19.97	20.47	19.79	19.14	18.77	18.73	18.37	18.22	18.02	17.91	99.00	17.92	17.96	17.65	17.31	21.28	19.12	17.71	17.96	17.71
2	350.53906250	16.87807274	0.056	2	18.81	18.14	17.90	17.46	17.11	16.89	16.64	16.51	16.29	16.21	16.21	16.02	15.90	15.83	15.65	18.90	17.37	16.55	16.12	15.81
3	350.53964233	16.80180168	0.025	7	19.67	18.74	18.76	18.87	18.76	18.78	18.73	18.59	18.59	18.46	18.61	18.57	18.41	18.95	18.30	20.28	18.78	18.83	18.64	17.51
4	350.54162598	16.67333031	0.033	3	17.46	17.12	16.89	16.80	16.70	16.64	16.63	16.59	16.27	16.29	16.56	16.42	16.43	16.32	16.44	17.64	16.83	16.59	16.38	16.31
5	350.54580688	17.26466942	0.044	1	18.43	18.17	17.35	16.98	16.61	16.48	16.12	16.05	15.82	15.84	15.83	15.58	15.48	15.41	15.29	18.65	16.88	16.08	15.71	15.40
6	350.55383301	16.42631340	0.030	4	99.00	17.89	17.36	17.30	17.17	17.09	17.01	16.94	16.64	16.68	16.78	16.67	16.62	16.51	16.42	18.28	17.38	16.91	16.72	16.53
7	350.56356812	16.40281296	0.057	1	99.00	19.14	18.76	18.34	17.92	17.67	17.50	17.38	17.12	17.11	17.02	16.83	16.74	16.65	16.59	20.31	18.26	17.32	16.91	16.70
8	350.58166504	16.80896950	0.046	3	99.00	19.30	19.08	19.27	19.09	19.00	18.84	18.76	18.47	18.42	18.83	18.39	18.20	17.90	18.04	27.70	19.21	18.70	18.44	18.47
9	350.59280396	16.95937729	0.027	2	21.58	20.38	20.05	20.26	19.60	19.54	19.30	19.37	19.17	19.00	19.23	19.09	18.62	18.73	18.58	21.78	19.96	19.39	19.01	18.84
10	350.59347534	17.01498795	0.061	1	18.23	18.19	17.76	17.08	16.59	16.36	16.04	15.92	15.67	15.61	15.56	15.34	15.28	15.19	15.02	18.86	16.91	15.98	15.53	15.21
11	350.59823608	17.03547859	0.060	4	18.41	18.12	17.76	17.67	17.47	17.34	17.20	17.13	17.01	16.74	17.01	16.81	16.77	16.76	16.68	18.65	17.63	17.17	16.84	16.73
12	350.60241699	17.10379982	0.049	1	19.14	18.44	17.81	17.45	17.06	16.95	16.61	16.51	16.30	16.28	16.26	16.04	15.95	15.88	15.78	19.16	17.34	16.55	16.17	15.87
13	350.61746216	16.42463112	0.023	1	99.00	20.87	23.37	21.43	20.31	20.35	19.81	19.77	19.44	19.95	19.31	19.61	19.63	18.89	19.21	21.89	20.76	19.95	19.44	19.11
14	350.63101196	16.37726974	0.048	1	99.00	20.15	20.43	18.97	19.07	19.17	18.84	18.77	18.34	18.68	99.00	18.76	18.60	18.93	18.08	21.33	20.02	18.94	18.48	18.07
15	350.63424683	16.78801537	0.017	1	19.89	19.24	20.16	19.33	18.95	18.87	18.54	18.42	18.16	18.04	17.96	17.83	17.70	17.72	17.48	20.93	19.24	18.43	17.92	17.62
16	350.63787842	16.44768906	0.034	1	99.00	18.21	18.07	17.93	17.80	17.77	17.71	17.68	17.49	17.48	17.61	17.59	17.45	17.26	17.38	19.08	17.91	17.62	17.52	17.63
17	350.66183472	16.35647392	0.053	1	99.00	18.22	19.08	18.75	18.23	18.05	17.84	17.77	17.48	17.38	17.45	17.31	17.12	17.09	17.09	20.48	18.57	17.74	17.35	17.08
18	350.66513062	16.86167526	0.024	3	17.74	17.16	16.55	16.31	16.00	15.89	15.59	15.48	15.21	15.20	15.11	15.00	14.85	14.73	14.68	17.75	16.24	15.47	15.06	14.74
19	350.68112183	16.36630630	0.037	1	99.00	18.48	18.64	18.42	18.31	18.25	18.14	18.03	17.87	17.76	18.11	17.87	17.75	17.87	17.70	19.81	18.33	18.05	17.81	17.88
20	350.74844360	17.16712379	0.043	1	18.98	18.49	17.84	17.45	17.04	16.91	16.57	16.48	16.28	16.25	16.19	15.97	15.91	15.79	15.74	19.21	17.31	16.51	16.12	15.82
21	350.75390625	16.79937553	0.024	2	19.40	17.97	17.70	17.55	17.37	17.32	17.22	17.13	16.90	16.86	16.93	16.86	16.79	16.66	16.61	18.74	17.49	17.09	16.85	16.73
22	350.75997925	17.14521217	0.039	3	19.86	19.90	19.73	20.21	19.71	19.59	19.28	19.20	18.92	19.17	18.94	18.87	18.52	18.41	18.72	21.14	19.85	19.22	18.91	18.76
23	350.76577759	16.54315758	0.049	1	20.30	20.17	20.00	19.01	18.83	18.77	18.41	18.44	18.28	18.27	18.29	18.16	18.24	18.04	18.40	20.72	19.24	18.01	18.31	18.09
24	350.77868652	17.10724640	0.024	1	20.60	19.35	19.24	19.50	19.68	19.58	19.74	19.38	19.15	19.26	19.36	19.24	18.96	18.83	18.27	20.94	19.65	19.26	19.09	19.02
25	350.78274536	16.53175163	0.044	1	18.69	17.89	16.86	15.96	15.78	15.60	15.09	14.93	14.69	14.55	14.42	14.30	14.22	14.11	14.08	17.71	15.79	14.75	14.54	15.16
26	350.79830933	16.60096359	0.043	1	21.28	20.15	19.27	19.26	19.10	19.09	18.99	18.93	18.85	18.82	19.27	18.91	18.58	18.54	19.00	21.02	19.26	18.85	18.62	18.75
27	350.80563354	16.58921432	0.031	1	18.68	18.03	17.76	17.80	17.64	17.56	17.55	17.48	17.24	17.24	17.33	17.26	17.14	17.26	17.15	18.95	17.79	17.48	17.28	17.13
28	350.82449341	16.66783524	0.049	1	20.62	19.83	19.37	19.16	18.85	18.71	99.00	18.54	18.33	18.26	18.43	18.27	18.22	18.15	17.70	20.33	19.10	18.59	18.35	18.10
29	350.82653809	17.22652817	0.039	2	18.35	18.39	17.60	17.49	17.24	17.10	16.78	16.71	16.49	16.47	16.45	16.25	16.18	16.08	16.02	18.79	17.39	16.71	16.34	16.12
30	350.82934570	16.66695786	0.042	1	99.00	19.18	22.12	21.04	20.26	19.84	19.63	19.42	19.39	19.38	19.75	19.36	18.77	18.94	18.26	21.60	20.64	19.74	19.32	18.99
31	350.83618164	16.79516220	0.044	2	18.94	18.48	18.03	17.98	17.76	17.69	17.57	17.51	17.31	17.34	17.34	17.24	17.16	17.15	17.20	19.11	17.95	17.53	17.28	17.10
32	350.85662842	16.77861404	0.026	4	19.63	19.39	19.17	19.20	19.10	19.08	18.82	18.77	18.67	18.67	18.45	18.57	18.13	18.28	18.15	20.28	19.18	18.71	18.46	18.30
33	350.87145996	16.61509132	0.030	1	99.00	21.13	21.10	19.81	19.79	19.72	19.44	19.09	18.92	19.01	19.11	19.02	18.78	18.99	18.28	21.46	19.95	19.30	18.94	18.74
34	350.87319946	16.90993500	0.048	5	18.74	17.81	17.28	17.19	17.00	16.93	16.74	16.67	16.38	16.39	16.55	16.40	16.33	16.26	16.18	18.01	17.12	16.71	16.53	16.03
35	350.87722778	16.76000595	0.031	1	20.83	19.47	18.77	18.22	17.91	17.83	17.53	17.46	17.20	17.12	17.13	17.00	16.84	16.76	16.81	19.82	18.19	17.42	17.07	16.79

Table 3
(Continued)

No.	R.A.	Decl.	z_{ph}	T	a	b	c	d	e	f	g	h	i	j	k	m	n	o	p	u'	g'	r'	i'	z'
36	350.88580322	17.04202461	0.059	3	99.00	20.15	19.62	19.63	19.33	19.19	18.86	18.66	18.42	18.42	18.61	18.18	18.24	18.16	18.08	21.35	19.19	18.80	18.40	22.37
37	350.89169312	16.81429672	0.050	3	20.64	99.00	19.21	19.50	19.07	18.98	18.75	18.59	18.03	18.36	18.32	18.21	18.01	18.14	17.76	20.76	19.36	18.63	18.28	18.07
38	350.89550781	16.77338600	0.023	1	19.77	19.65	18.79	18.77	18.44	18.39	18.15	17.99	17.82	17.80	17.67	17.67	17.49	17.35	17.53	20.36	18.68	17.97	17.63	17.39
39	350.90295410	16.65809059	0.034	1	19.60	18.60	18.01	17.57	17.16	17.07	16.79	16.69	16.48	16.47	16.41	16.25	16.10	16.07	15.95	19.16	17.46	16.70	16.34	16.04
40	350.90997314	17.03512764	0.044	4	20.55	19.23	20.50	20.07	19.66	19.58	19.49	19.47	19.30	19.37	19.41	19.05	18.89	18.43	19.26	21.03	19.95	19.41	19.07	18.88
41	350.91564941	17.15081024	0.024	4	99.00	19.85	19.81	19.91	19.96	19.89	19.78	19.61	19.29	19.39	19.48	19.46	19.15	19.57	18.51	20.45	20.02	19.47	19.14	20.33
42	350.92758179	16.63711929	0.038	1	99.00	21.10	19.45	18.70	18.50	18.36	18.15	17.99	17.71	17.69	17.66	17.54	17.33	17.31	17.10	20.44	18.71	17.91	17.54	17.35
43	350.93566895	16.57441330	0.056	1	19.92	19.62	19.04	18.54	18.12	18.04	17.80	17.68	17.42	17.34	17.40	17.20	17.10	17.16	16.93	20.17	18.46	17.69	17.34	17.03
44	350.94158936	16.53168869	0.018	1	99.00	20.07	20.71	21.04	19.87	20.02	19.49	19.44	18.90	19.61	18.81	18.88	18.96	18.52	18.77	21.69	20.28	19.41	18.99	18.63
45	350.94189453	16.83019829	0.043	1	19.53	18.82	18.11	17.73	17.31	17.21	16.91	16.78	16.57	16.51	16.53	16.30	16.17	16.04	16.02	19.43	17.59	16.75	16.35	16.08
46	350.94229126	16.98780251	0.028	4	19.98	19.84	20.99	19.90	19.57	19.54	19.20	19.47	19.32	19.30	19.21	19.18	19.03	18.43	19.84	20.88	19.91	19.34	18.95	18.75
47	350.95550537	17.13400650	0.040	1	20.20	19.64	19.98	19.63	19.49	19.50	19.22	19.04	18.86	18.90	18.90	18.62	18.50	18.74	18.44	21.48	19.73	19.14	18.78	18.45
48	350.95840454	16.35474205	0.053	1	20.36	20.85	21.16	20.08	19.73	19.67	19.17	19.66	19.24	18.83	19.62	19.04	18.93	19.11	18.84	21.15	20.14	19.62	19.16	19.02
49	350.96127319	16.79039574	0.053	2	19.94	21.01	19.55	21.15	20.47	20.73	20.44	20.40	19.45	19.56	19.72	19.51	19.46	19.79	19.08	22.11	21.00	20.14	19.80	19.44
50	350.96603394	16.67181778	0.045	1	20.55	19.06	18.82	18.18	17.82	17.72	17.45	17.30	17.11	17.09	17.03	16.85	16.75	16.66	16.79	19.93	18.12	17.32	16.95	16.64
51	350.96640015	17.02894592	0.026	3	19.82	19.08	19.00	18.88	18.63	18.58	18.36	18.37	18.24	18.14	18.20	18.16	18.15	17.83	18.14	20.05	18.76	18.53	18.06	17.97
52	350.96762085	16.92559433	0.053	1	22.61	19.19	18.74	18.29	17.92	17.81	17.47	17.39	17.20	17.23	17.07	16.92	16.85	16.77	16.68	20.24	18.25	17.09	17.09	16.80
53	350.97122192	16.77782631	0.046	1	22.02	99.00	18.92	18.75	18.30	18.23	17.96	17.80	17.69	17.48	17.53	17.41	17.28	17.15	17.14	20.27	18.62	17.81	17.42	17.17
54	350.97134399	16.73224449	0.036	3	20.68	99.00	20.16	19.77	19.69	19.56	19.49	19.35	19.41	18.94	19.12	18.96	18.85	18.66	18.91	21.10	19.82	19.28	18.95	18.81
55	350.97305298	16.64459801	0.045	3	22.17	99.00	20.97	20.47	19.80	20.08	20.28	19.58	19.32	19.46	20.45	19.37	19.84	18.82	18.59	23.03	20.17	19.60	19.32	19.23
56	350.97525024	16.46105576	0.053	1	99.00	20.26	20.66	19.56	19.05	18.75	18.52	18.39	18.17	18.07	18.15	17.90	17.71	17.54	17.92	21.26	19.35	18.37	17.96	17.63
57	350.97549438	16.53599358	0.046	1	99.00	20.10	19.03	18.94	18.59	18.47	18.19	18.08	17.90	17.80	17.79	17.66	17.53	17.48	17.54	20.27	18.81	18.10	17.75	17.50
58	350.99014282	16.72022820	0.052	1	21.11	20.54	20.19	20.41	20.04	19.83	19.66	19.26	19.25	19.02	19.64	18.89	18.71	19.04	18.41	21.44	20.16	19.42	19.12	19.03
59	351.00198364	16.89023781	0.060	2	19.89	19.15	20.41	19.69	19.18	19.08	18.74	18.83	18.55	18.87	18.73	18.31	18.27	18.25	18.29	21.27	19.50	18.81	18.47	18.25
60	351.00668335	17.24337769	0.046	7	19.61	19.78	19.50	19.50	19.58	19.54	19.48	19.29	19.32	18.99	19.80	19.10	19.53	18.56	18.72	20.64	19.50	19.32	19.09	19.51
61	351.00845337	16.75835037	0.021	1	20.54	99.00	18.60	18.87	18.46	18.36	18.09	17.94	17.76	17.75	17.61	17.54	17.40	17.24	17.35	20.46	18.73	17.96	17.61	17.29
62	351.01538086	16.60781860	0.058	1	21.07	19.52	18.94	18.65	18.25	18.12	17.87	17.75	17.54	17.45	17.46	17.25	17.21	17.11	17.00	20.48	18.61	17.45	17.47	17.14
63	351.01727295	16.77843475	0.024	3	20.25	19.79	99.00	19.56	19.27	19.35	19.02	18.93	18.68	18.71	18.65	18.68	18.43	18.67	18.49	25.43	19.59	18.92	18.59	18.56
64	351.02890015	16.76558304	0.020	1	20.00	22.55	20.23	19.93	19.76	19.77	19.47	19.31	18.71	19.26	18.88	18.92	18.80	19.19	18.37	21.94	20.02	19.23	18.91	18.68
65	351.03451538	16.70536232	0.035	3	99.00	18.89	20.16	20.05	19.87	19.88	19.71	19.35	19.21	19.51	19.07	19.08	18.55	18.87	18.28	21.10	20.01	19.31	19.08	18.77
66	351.03710938	16.74093056	0.023	2	23.21	19.34	19.10	19.17	18.77	18.71	18.39	18.26	18.15	18.14	18.04	17.89	17.85	17.67	17.53	20.59	19.08	18.37	17.91	17.68
67	351.05773926	17.07377625	0.042	3	20.37	99.00	19.75	20.35	19.93	20.02	20.09	19.51	19.24	19.22	20.10	19.33	18.87	19.21	17.99	21.51	20.19	19.51	19.16	19.09
68	351.05862427	16.73395157	0.039	2	20.61	19.17	18.44	18.03	17.71	17.64	17.36	17.23	17.07	17.08	16.98	16.86	16.64	16.56	16.57	19.48	17.91	17.20	16.93	16.70
69	351.06436157	16.63640594	0.030	4	19.44	18.88	19.31	18.93	18.71	18.66	18.38	18.44	18.26	18.23	18.29	18.08	18.03	17.76	17.92	20.03	18.89	18.43	18.09	17.84
70	351.07086182	16.99158096	0.024	1	99.00	20.32	19.20	19.63	19.40	19.30	18.90	18.90	18.77	18.77	18.69	18.66	18.44	18.34	18.28	21.00	19.61	18.89	18.59	18.36

Table 3
(Continued)

No.	R.A.	Decl.	z_{ph}	T	a	b	c	d	e	f	g	h	i	j	k	m	n	o	p	u'	g'	r'	i'	z'
71	351.07095337	16.57386208	0.044	1	19.72	19.19	18.01	17.58	17.19	17.06	16.79	16.67	16.47	16.43	16.38	16.22	16.10	15.99	15.91	19.23	17.46	16.68	16.28	16.00
72	351.07333374	17.14213371	0.049	4	19.34	18.67	18.68	18.73	18.49	18.29	18.31	18.24	17.95	17.77	18.06	17.91	17.85	17.98	17.91	19.72	18.69	18.30	17.97	17.78
73	351.08377075	16.50154114	0.048	1	19.22	19.18	19.89	19.37	19.31	19.35	19.23	19.10	18.81	18.54	19.12	18.79	18.97	19.08	19.04	20.57	19.52	19.15	18.94	18.91
74	351.08947754	17.21441841	0.017	3	20.79	21.03	20.33	20.30	19.88	20.04	19.59	19.61	19.30	19.23	19.33	19.16	19.05	19.37	19.14	21.53	20.25	19.62	19.25	18.87
75	351.09808350	16.88235664	0.057	1	19.18	19.37	19.29	18.75	18.43	18.26	18.02	17.90	17.71	17.73	17.64	17.46	17.35	17.42	17.32	20.40	18.63	17.87	17.71	17.23
76	351.11566162	16.69385719	0.047	1	19.95	19.04	18.35	18.00	17.59	17.47	17.23	17.10	16.87	16.87	16.80	16.62	16.48	16.46	16.35	19.61	17.89	17.10	16.71	16.43
77	351.11795044	16.47721481	0.023	3	19.64	21.00	20.46	20.28	19.91	20.04	19.73	19.37	19.21	19.47	19.24	19.00	18.83	18.61	19.61	21.22	20.05	19.43	19.09	18.86
78	351.12063599	16.41191292	0.060	3	19.79	19.44	19.54	19.19	18.93	18.75	18.57	18.52	18.25	18.18	18.31	18.07	17.85	17.89	17.78	20.45	19.19	18.42	18.19	17.93
79	351.12286377	17.11305428	0.048	3	99.00	19.32	20.58	19.98	19.77	19.77	19.66	19.32	19.38	19.04	19.26	18.92	18.64	19.10	18.72	21.28	20.00	19.36	19.06	18.91
80	351.12655640	16.86726189	0.050	3	19.86	18.40	17.88	17.72	17.60	17.59	17.54	17.48	17.17	17.26	17.34	17.25	17.16	17.31	17.31	17.09	17.57	17.53	17.53	16.89
81	351.13357544	16.66821671	0.042	1	19.57	19.08	18.33	17.97	17.67	17.60	17.34	17.20	17.01	16.95	16.95	16.77	16.67	16.59	16.54	19.50	17.92	17.22	16.82	16.57
82	351.16860962	16.48097610	0.056	4	19.08	19.39	18.77	18.76	18.49	18.43	18.27	18.16	17.88	17.88	17.93	17.67	17.71	17.54	17.48	19.97	18.69	18.12	17.81	17.60
83	351.17163086	16.57984734	0.048	3	21.16	20.21	20.15	19.50	19.25	19.19	18.87	18.84	18.74	18.41	18.43	18.32	18.20	18.11	18.37	20.77	19.48	18.74	18.41	18.16
84	351.21090698	17.24355888	0.060	2	18.82	20.16	19.54	19.82	19.45	19.15	18.99	19.05	18.80	18.59	18.87	18.61	18.81	18.13	18.34	20.96	19.72	18.91	18.79	18.52
85	351.21206665	16.90178680	0.048	1	21.39	19.59	19.38	19.17	18.73	18.62	18.33	18.22	18.03	17.91	17.89	17.79	17.67	17.55	17.29	20.60	19.01	18.05	17.89	17.62
86	351.21966553	16.53191757	0.059	3	19.22	20.53	19.63	19.52	19.03	19.04	19.05	18.67	18.57	18.56	18.40	18.33	18.17	18.28	18.47	24.55	19.46	18.71	18.36	18.12
87	351.22222900	16.40045166	0.017	1	19.30	99.00	19.30	19.94	19.47	19.41	19.31	19.02	18.90	18.56	18.72	18.73	18.60	18.16	18.12	22.09	19.75	19.01	18.69	18.38
88	351.24563599	16.71162224	0.047	3	20.25	19.46	18.89	18.53	18.23	18.14	17.91	17.86	17.61	17.62	17.55	17.47	17.40	17.09	17.14	19.66	18.42	17.82	17.50	17.35
89	351.24801636	17.16534615	0.024	1	23.67	20.18	19.45	19.96	19.62	19.56	19.20	19.13	18.91	18.95	18.70	18.55	18.52	18.26	17.96	21.47	19.93	19.07	18.62	18.38
90	351.26184082	16.57231903	0.023	3	18.84	20.03	20.31	20.80	20.38	20.48	19.75	19.87	19.41	19.58	19.46	19.47	18.72	19.29	99.00	21.78	20.48	19.83	19.44	19.17
91	351.26245117	16.52570343	0.024	1	99.00	99.00	21.90	21.17	20.25	20.81	20.70	19.87	19.49	20.36	19.56	19.69	19.63	99.00	19.79	21.82	20.60	19.96	19.81	19.55
92	351.27828979	16.76721191	0.044	1	19.06	18.34	17.96	17.76	17.63	17.57	17.44	17.36	17.19	17.24	17.24	17.11	17.04	16.98	17.24	19.02	17.72	17.33	17.13	17.03
93	351.28054810	16.81988525	0.029	1	19.76	21.59	19.68	19.32	19.33	19.17	18.97	19.06	18.78	19.34	18.74	18.81	18.52	19.08	19.11	20.63	19.61	19.02	18.82	18.59
94	351.30871582	16.44901848	0.024	2	18.91	19.99	19.60	19.39	19.18	19.07	18.98	18.66	18.48	18.47	18.37	18.25	18.15	17.96	18.00	19.73	19.32	18.69	18.27	18.02
95	351.31192017	16.55031013	0.017	1	19.12	20.74	19.24	18.62	18.41	18.37	17.88	17.83	17.64	17.57	17.59	17.47	17.42	17.29	17.33	20.57	18.61	17.81	17.50	17.33
96	351.36566162	17.25617027	0.048	7	99.00	20.54	21.00	20.06	19.55	19.86	19.31	19.08	19.26	19.51	19.51	19.36	18.81	19.88	19.17	20.47	19.86	19.60	19.51	19.08
97	351.40484619	17.24501801	0.037	2	20.47	20.04	19.57	19.46	19.07	19.01	18.73	18.61	18.37	18.26	18.23	17.94	17.97	18.00	18.11	21.97	19.22	18.56	18.25	18.03
98	351.41052246	16.57383156	0.048	3	20.84	20.53	20.54	19.65	19.35	19.23	99.00	18.92	18.79	18.55	18.84	99.00	18.38	18.14	18.30	20.70	19.60	18.88	18.54	18.24
99	351.41250610	17.13726997	0.045	3	20.05	19.68	19.11	19.24	18.84	18.54	18.43	18.31	18.14	18.18	17.83	17.90	17.80	17.93	17.88	26.46	19.04	18.33	17.97	17.69
100	351.42208862	16.75362396	0.029	1	19.70	20.91	20.45	19.74	19.97	19.86	19.42	19.17	19.08	19.25	18.85	99.00	18.47	18.67	19.07	21.26	20.19	19.20	18.86	18.47
101	351.42596436	16.77386093	0.039	4	19.45	19.22	20.35	19.36	19.23	19.17	18.87	19.01	18.88	18.52	18.62	99.00	18.30	18.49	18.30	20.22	19.36	18.88	18.56	18.54
102	351.42956543	16.78918457	0.046	3	19.33	23.81	20.52	20.13	19.69	19.60	19.31	19.47	19.41	19.18	19.42	99.00	18.68	18.80	19.43	21.38	20.04	19.38	18.97	18.86
103	351.43093872	16.47374535	0.048	3	19.44	23.05	20.24	19.95	19.51	19.50	19.02	19.08	18.80	18.71	18.94	99.00	18.46	18.86	18.50	21.30	19.84	19.16	18.86	18.53
104	351.45364380	16.79960823	0.018	2	99.00	99.00	19.24	19.30	19.18	19.10	18.81	18.77	18.66	18.29	18.40	99.00	18.18	17.97	17.96	20.85	19.39	18.67	18.35	18.08
105	351.45440674	16.41203117	0.029	7	19.82	19.38	19.05	19.26	19.08	18.99	18.90	19.03	18.79	18.89	18.90	99.00	18.67	18.62	18.37	21.07	19.22	18.97	18.79	18.68
106	351.46267700	16.88102722	0.058	3	99.00	20.35	20.28	19.93	19.58	19.59	19.24	19.39	19.26	19.57	19.22	99.00	18.70	19.15	19.89	23.66	19.82	19.35	19.09	19.06

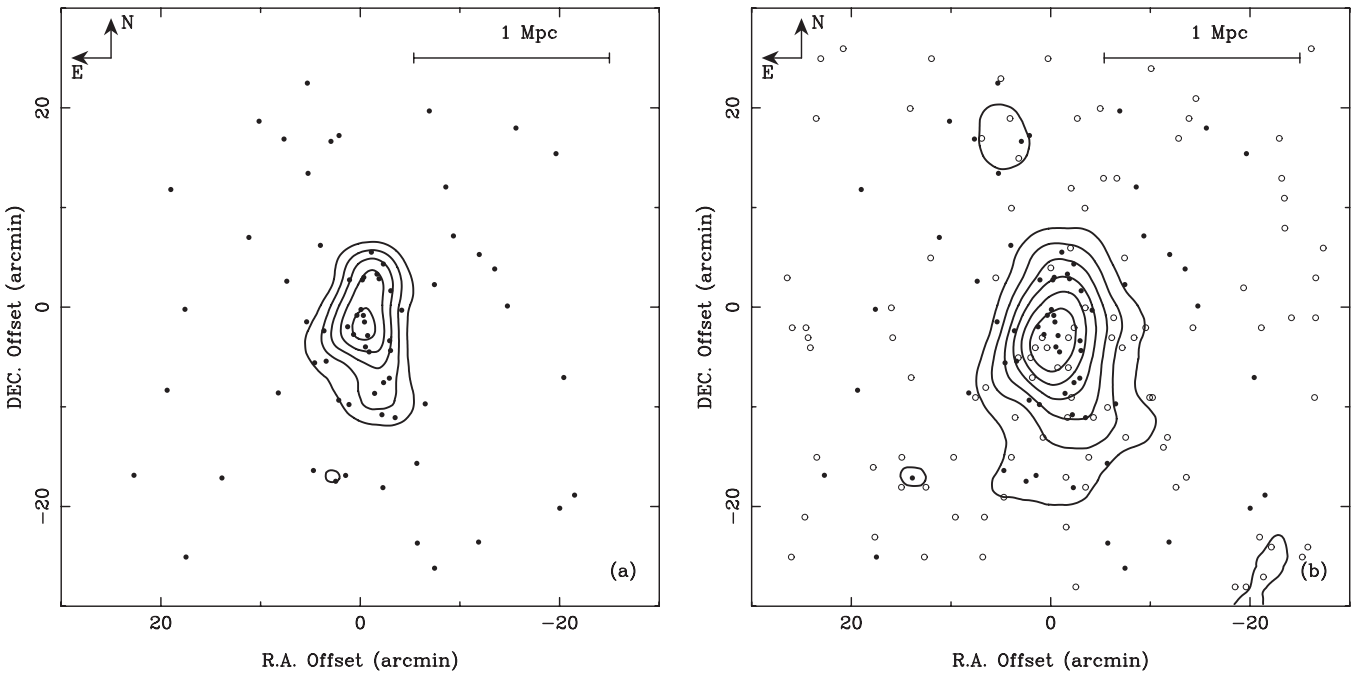

Figure 10. Left: spatial distribution for 68 spectroscopic member galaxies of A2589 in sample I. The contour map of the surface density uses the smoothing Gaussian window $\sigma = 3'$. Right: spatial distribution for 171 member galaxies in sample II. The smoothing Gaussian window is $\sigma = 4'$. For both panels, the contour levels are 0.09, 0.14, 0.19, 0.24, 0.29, and 0.34 arcmin^{-2}, respectively.

Table 4
Results of the κ-test for Member Galaxies in Samples I and II

Neighbor Size n	Sample I $P(\kappa_n > \kappa_n^{\rm obs})$	Sample II $P(\kappa_n > \kappa_n^{\rm obs})$
6.....	84.8%	17.8%
7.....	85.9%	21.4%
8.....	81.9%	13.8%
9.....	87.8%	14.5%
10.....	85.2%	21.7%
11.....	85.9%	31.2%
12.....	79.9%	49.2%

indicating that the local velocity distribution is in accordance with the overall one. Even for the enlarged sample II, bubble clustering at the center is still negligible. A close comparison between the projected distribution (in Figure 10) and bubble plot (in Figure 11) shows that A2589 is a well-relaxed cluster with no dynamic substructures detected both in two-dimensional mapping and in radial velocity space.

An elongation along the north–south direction has been unveiled in Figure 10. To verify whether a substructure exists at about 10 arcmin south of the main concentration, we further apply a technique of mixture modeling, namely, the KMM algorithm, to samples I and II. The KMM is a maximum-likelihood algorithm which assigns objects into groups and assesses the improvement in fitting a multigroup over a single group model (Ashman et al. 1994). Based on the three-dimensional data (i.e., projected positions and radial velocities of member galaxies), we set the initial positions: (0.0, 0.0) for the main concentration and (−2.0, −11.0) for the possible substructure, and the initial mean velocities are 12,050 km s^{-1} for two clumps. The KMM algorithm gives the following optimum two-group solutions: only three galaxies in sample I are assigned as members of the southern substructure, and only five galaxies in sample II are allocated to the substructure. This means that the southern abnormal feature in projected mapping is not a significant substructure, which supports the conclusion drawn by the κ-test that no significant dynamic substructures are found in A2589.

4.3. Luminosity Function

The LF is a fundamental tool for analyzing the properties of galaxies in a cluster. Usually, a Gaussian function can be used to describe the LF of bright galaxies with $i < 19.0$ mag (Binggeli et al. 1988) $N(M) \sim \exp[-(M-\mu)^2/2\sigma^2]$, where μ is the characteristic absolute magnitude and σ is the dispersion. For the faint galaxies with $i > 19.0$ mag, a Schechter function is needed to give a better fit (Schechter 1976): $N(M) = \phi^*[10^{-0.4(M-M^*)}]^{(\alpha+1)} e^{-10^{-0.4(M-M^*)}}$, where ϕ^*, M^*, and α are the normalization parameter, the characteristic absolute magnitude, and the slope at the faint end, respectively. For the cluster galaxies, a single Schechter function cannot give a perfect description of the LFs (Driver et al. 1994; Mohr et al. 1996; Trentham & Tully 2002; Yang et al. 2004). Ferguson & Sandage (1991) performed an LF fitting with these two functions.

For comparison with previous results, the BATC magnitudes were converted into the conventional Kron–Cousins magnitudes via the equations in Zhou et al. (2003). The M_R magnitudes in sample II cover a range from −22.0 to −16.5 mag, and a turnoff point at $M_R = -18.75$ is found in magnitude distribution. We use the combination of above two functions to describe the LFs of galaxies in A2589: a Gaussian function for the bright galaxies, and a Schechter function for the faint galaxies. The fitting results in a Gaussian function with $\mu = -20.0^{+0.02}_{-0.18}$, $\sigma = -1.34^{+0.02}_{-0.02}$, and a Schechter function with $M^* = -17.8^{+0.35}_{-0.01}$, $\alpha = -0.53^{+0.20}_{-0.04}$. The combination of two functions gives a good description for the LFs of A2589 (see Figure 12).

Though the uncertainty in member selection might be larger for faint galaxies, the LF peak at $M_R \sim -20$ and dip at $M_R \sim -19$ might be real because the BATC photometry is capable of detecting galaxies brighter than 19.5 mag. With the

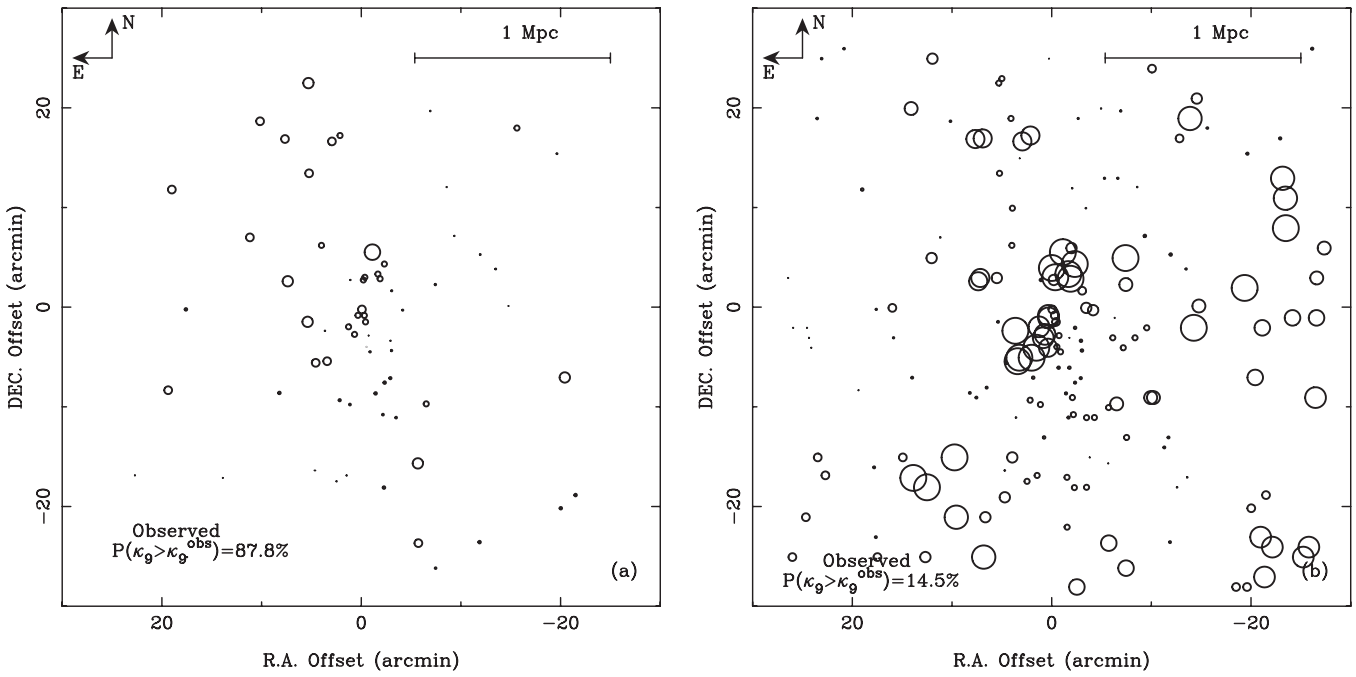

Figure 11. (a) Bubble plot showing the localized variation for groups of the nine nearest neighbors for (a) 68 galaxies in sample I and (b) 174 galaxies in sample II.

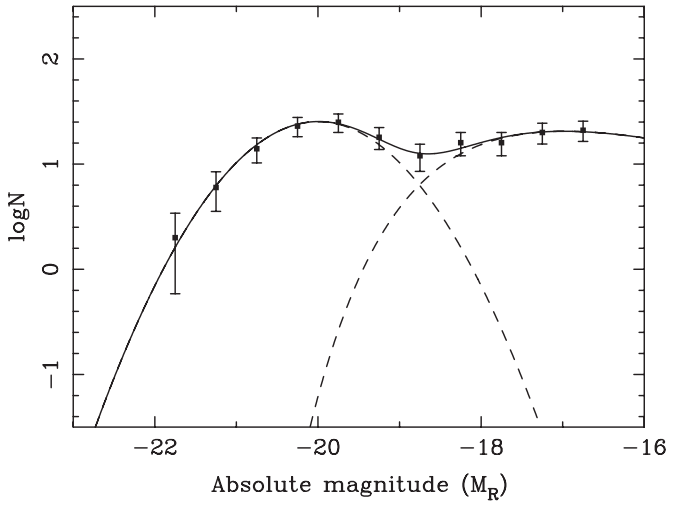

Figure 12. Observed LF of the *R* band. The dashed lines indicate the components of the Gauss and Schechter function and the solid lines are their sum.

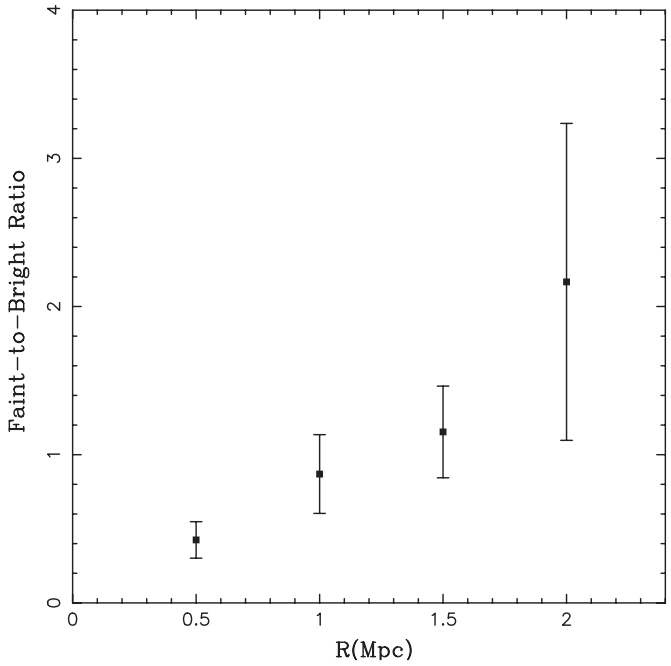

Figure 13. Faint-to-bright ratio (FBR) as a function of the clustercentric distance of A2589. The mean FBRs are computed in annuli of 0.5 Mpc width.

clear peak at $M_R \sim -20$, the bright part of the LF of A2589 looks similar to an LF of rich clusters, which have a bump in the bright part (Biviano et al. 1995). Our turnoff magnitude $M_R = -18.75$ is similar to the LFs in A963 (Driver et al. 1994), Coma (Thompson & Gregory 1993), and A2554 (Smith et al. 1997). For the LF slope at faint parameter α, A2589 has a flatter slope than many rich clusters, which might be due to the incompleteness in the selection of faint members.

Following the definition of the dwarf-to-giant ratio in Driver et al. (1998), we define the faint-to-bright ratio (FBR) as the count ratio of faint galaxies to bright galaxies, FBR $= \sum N(M_R > -18.75) / \sum N(M_R < -18.75)$. The overall FBR is about 0.84. It is found that the FBR varies with clustercentric radius: FBR $= 0.44$ in the central region ($R \leqslant 0.5$ Mpc) and FBR $= 1.23$ in the outer region ($R > 0.5$ Mpc). The increasing tendency of the FBR along the radial distance is presented in Figure 13. Obviously, the faint end of the LF is dominated by faint/dwarf galaxies, which can be interpreted by the "dwarf population density" relation (Phillipps et al. 1998): dwarf galaxies are more common in a low-density environment. This segregation may originate from the initial conditions of the formation of dwarf galaxies, where low-luminosity galaxies are only now in-falling into clusters (Croton et al. 2005), or the galaxies may have suffered processes internal to clusters, such as tidal disruption and galaxy harassment (Mastropietro et al. 2005; Aguerri et al. 2004, 2005), and consequently dimmed.

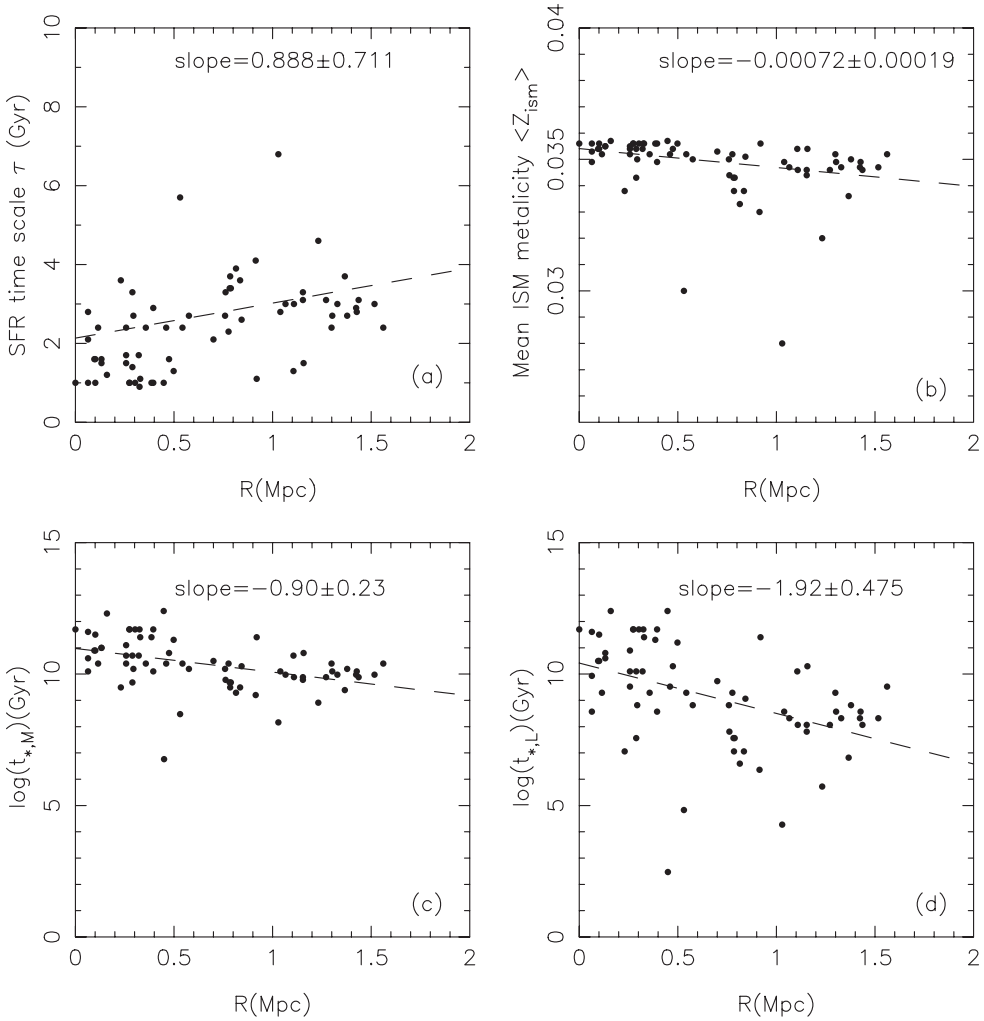

Figure 14. Star formation properties for the galaxies with known z_{sp} in A2589 as a function of the project radius R. The star formation properties are the SFR timescale τ, mean ISM metallicity, and the mean stellar ages weighted by mass and light.

4.4. Star Formation Properties of Cluster Galaxies

The star formation histories of the member galaxies can provide important clues for understanding the evolution of their host cluster. For a cluster galaxy, both the cluster-scale gravity environment and the galaxy-scale interaction may have influenced the physical processes concerning star formation. Therefore, it is interesting to observe the systematic tendency of the star formation properties for the galaxies in a cluster.

With an evolution synthesis model, PEGASE (version 2.0; Fioc & Rocca-Volmerange 1997, 1999), the star formation properties of A2589 are investigated. We assume a Salpeter (1955) initial mass function (IMF) and a star formation rate (SFR) in exponentially decreasing form, SFR(t) $\propto e^{-t/\tau}$, where the timescale τ ranges from 0.5 to 30.0 Gyr. To avoid degeneracy between age and metallicity in the model, we use the same age of 12.86 Gyr for all the member galaxies in A2589, responding to the age of the first generation stars at $z_c = 0.0414$. A zero initial metallicity of the interstellar medium (ISM) is assumed. First, a series of rest-frame modeled spectra at $z = 0$ with various star formation histories is generated by running the PEGASE code. Then we shift them to the observer's frame for a given redshift, and then convolve with the transmission functions of the BATC and SDSS filters. As a result, we obtain the template SED library containing the BATC and SDSS photometric bands.

Based on the template SED library, we search for the minimal χ^2 fit of the observed SEDs of 68 bright member galaxies with known spectroscopic redshifts. The SFR timescale (τ), mean ISM metallicity ($Z_{\rm ISM}$), and the mean stellar age ($t_\star$) weighted by mass and light can be achieved.

Figure 14 shows the star formation properties as a function of the projected radius (R) for 68 member galaxies in sample I. The dashed lines denote the best linear fitting results. Panel (a) shows that the SFR timescale is shorter in the inner region than that in the outer region. This result agrees with the morphology–density relation pointed out by Dressler (1980), which can be well explained in the context of a hierarchical cosmological scenario (Poggianti 2004). Panel (b) shows that the outlier galaxies have a higher probability of having a lower metallicity, which is consistent with the picture that more massive galaxies form fractionally more stars in a Hubble time than their low-mass counterparts, and metals are selectively lost from the faint galaxies with shallow potential wells via galactic winds (Tremonti et al. 2004). Panels (c) and (d) show that the galaxies in the core region tend to possess an older stellar population with longer mean stellar ages weighted by either mass or light. A comparison between panels (c) and (d) shows that the gradient of the light-weighted stellar age is steeper. After the evolution of galaxies, stellar mass is dominated by an old stellar population with dimmed light. On the other hand, the

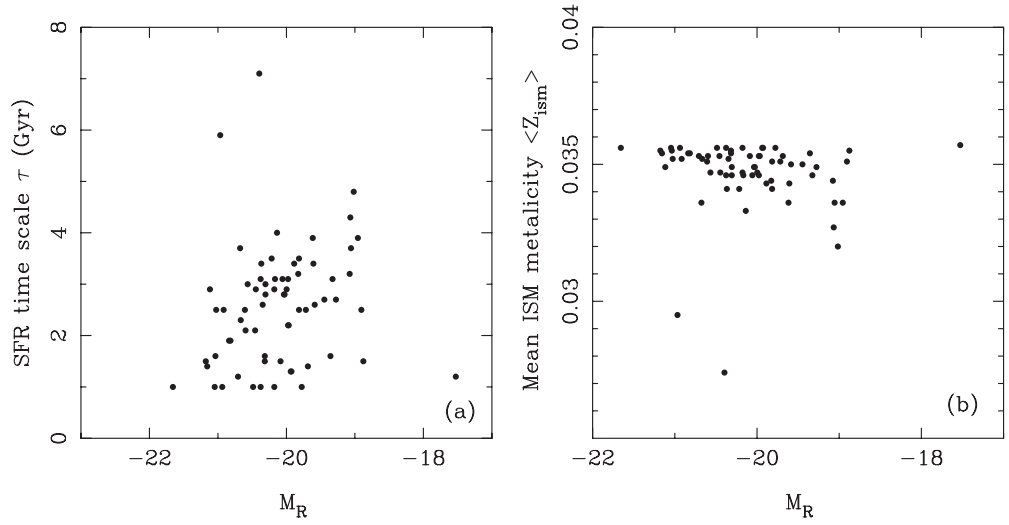

Figure 15. SFR timescale τ and mean ISM metallicities for the galaxies with known z_{sp} in A2589 as a function of magnitude in the *R* band.

current SFR in a cluster is mainly due to the late-type galaxies in the outer region, and the younger stellar population has a greater weight in mean age calculation. It is reasonable that the stellar ages weighted by bolometric luminosity tend to be younger for the outlier galaxies.

Figure 15 gives the SFR timescale τ and the ISM metallicities as a function of absolute magnitude (M_R). The high-luminosity galaxies tend to have shorter timescales. For the bright and massive cluster galaxies in the core region of A2589, their star formation activities might have been reduced by many different physical processes via environmental effects, such as galaxy–galaxy interaction, harassment, gas stripping, and strangulation (Poggianti 2004; Yuan et al. 2005), which results in a short timescale of star formation.

5. SUMMARY

We present our multicolor optical photometry for the nearby regular cluster of galaxies A2589, based on the BATC 15 intermediate band system and SDSS photometric data. The SEDs in 15 bands were obtained for more than 5000 sources detected from ∼1 deg^2 of the BATC images. After cross-identifying the BATC sources with the SDSS photometric catalog, 1199 galaxies were extracted. An interpolation method was performed for a zero-point correction, and the combined 20 band SEDs for 1199 galaxies were archived. Then, a photometric redshift technique and the CM relation of early-type galaxies were applied to select fainter member galaxies. As a result, 106 galaxies were selected as faint member galaxies. Combining 68 member galaxies with known spectroscopic redshifts (i.e., sample I), we obtained an enlarged sample of 174 member galaxies (i.e., sample II).

The projected distribution shows no prominent clumps. The contour of surface density shows a north–south elongation, which agrees with the X-ray brightness profile and the orientation of the central cD galaxy, NGC 7647. A subsequent κ-test also indicated no substructure in the galaxy cluster A2589, which agrees with the X-ray images by *ROSAT* (Buote & Tsai 1996) and *Chandra* (Buote & Lewis 2004). Our conclusion is that A2589 is a well-virialized and relaxed system.

The LF of member galaxies in A2589 shows a peak at $M_R \sim -20.0$ and a dip at $M_R \sim -19.0$. Compared with other clusters, the turnoff point seems to be independent of the richness and dynamic stage. The FBR increases monotonously along a clustercentric distance, indicating that the faint and dwarf galaxies tend to be located in the outer region of a cluster.

The star formation properties of cluster galaxies unveil an environmental influence on the evolution of A2589. Bright and massive galaxies in the core region are found to have shorter SFR timescales, longer mean stellar ages, and higher mean ISM metallicities, while the outlier galaxies are likely to have smaller stellar ages and longer SFR timescales. These results can be well interpreted by the existing correlations, such as the morphology–density relation, the luminosity–metallicity relation, and the mass–metallicity relation.

We thank the anonymous referee for his/her invaluable comments and suggestions. This work was funded by the National Natural Science Foundation of China (NSFC; grants 10778618, 10633020, 10873016, 10603006, and 10803007) and the National Basic Research Program of China (973 Program, grant 2007CB815403). This research has made use of the NED, which is operated by the Jet Propulsion Laboratory, California Institute of Technology, under contract with the National Aeronautics and Space Administration. We thank Professors X. Kong and F.-Z. Cheng at the University of Science and Technology of China for their valuable discussions.

REFERENCES

Abell, G. O. 1958, ApJS, 3, 211
Adami, C., et al. 2009, A&A, 507, 1225
Aguerri, J. A. L., Gerhard, O. E., Arnaboldi, M., Napolitano, N. R., Castro-Rodriguez, N., & Freeman, K. C. 2005, AJ, 129, 2585
Aguerri, J. A. L., Iglesias-Paramo, J., Vilchez, J. M., & Muñoz-Tuñón, C. 2004, AJ, 127, 1344
Allen, D. A. 1976, MNRAS, 174, 29
Arnouts, S., et al. 1999, MNRAS, 310, 540
Ashman, K. M., Bird, C. M., & Zept, S. E. 1994, AJ, 108, 2348
Bahcall, N. A. 1999, in New Worlds in Astroparticle Physics II, ed. A. M. Mourão, M. Pimenta, & P. Sá (Singapore: World Scientific), 77
Bauer, F. E., Condon, J. J., Thuan, T. X., & Broderick, J. J. 2000, ApJS, 129, 547
Bautz, L. P., & Morgan, W. W. 1970, ApJ, 162, L149
Beers, T. C., Flynn, K., & Gebhardt, K. 1990, AJ, 100, 32
Beers, T. C., Gebhardt, K., Forman, W., Huchra, J. P., & Jones, C. 1991, AJ, 102, 1581
Bekki, K. 2001, Ap&SS, 276, 1033
Binggeli, B., Sandage, A., & Tammann, G. A. 1988, ARA&A, 26, 509
Biviano, A., Durret, F., Gerbal, D., Le Fevre, O., Lobo, C., Mazure, A., & Slezak, E. 1995, A&A, 297, 610
Bolzonella, M., Miralles, J.-M., & Pelló, R. 2000, A&A, 363, 476

Bothun, G. D., & Schombert, J. M. 1988, ApJ, 335, 617
Bower, R. G., Lucey, J. R., & Ellis, R. S. 1992, MNRAS, 254, 589
Bower, T. C., & Balogh, M. L. 2004, in Clusters of Galaxies: Probe of Cosmological Structure and Galaxy Evolution, ed. J. S. Mulchaey, A. Dressler, & A. Oemler (Cambridge: Cambridge Univ. Press), 326
Bruzual, A. G., & Charlot, S. 1993, ApJ, 405, 538
Buote, D. A., & Lewis, A. D. 2004, ApJ, 604, 116
Buote, D. A., & Tsai, J. C. 1996, ApJ, 458, 27
Burns, J. O., Rhee, G., Owen, F. N., & Pinkney, J. 1994, ApJ, 423, 94
Capelato, H. V., Mazure, A., Proust, D., Vanderriest, C., Lemonnier, J. P., & Sodre, L., Jr. 1991, A&AS, 90, 355
Cen, R., & Ostriker, J. 1994, ApJ, 429, 4
Colless, M., & Dunn, A. M. 1996, ApJ, 458, 435
Croton, D. J., et al. 2005, MNRAS, 356, 1155
David, L. P., Jones, C., & Forman, W. 1996, ApJ, 473, 692
Dressler, A. 1980, ApJS, 42, 565
Driver, S. P., Couch, W. J., & Phillipps, S. 1998, MNRAS, 301, 369
Driver, S. P., Phillipps, S., Davies, J. I., Morgan, I., & Disney, M. J. 1994, MNRAS, 268, 393
Evrard, A. E. 1989, ApJ, 341, L71
Fan, X., et al. 1996, AJ, 112, 628
Ferguson, H. C., & Sandage, A. 1991, AJ, 101, 765
Fioc, M., & Rocca-Volmerange, B. 1997, A&A, 326, 950
Fioc, M., & Rocca-Volmerange, B. 1999, A&A, 351, 869
Forman, W., & Jones, C. 1982, ARA&A, 20, 547
Frenk, C. S., White, S. D. M., Efstathiou, G., & Davis, M. 1990, ApJ, 351, 10
Frenk, C. S., et al. 1996, ApJ, 472, 146
Furusawa, H., Shimasaku, K., Doi, M., & Okamura, S. 2000, ApJ, 534, 624
Gunn, J. E., & Stryker, L. L. 1983, ApJS, 52, 121
Haynes, M. P., Giovanelli, R., Herter, T., Vogt, N. P., Freudling, W., Maia, M. A. G., Salzer, J. J., & Wegner, G. 1997, AJ, 113, 1197
Henry, J. P., & Briel, U. G. 1993, Adv. Space Res., 13, 191
Jenkner, H., Lasker, B. M., Sturch, C. R., McLean, B. J., Shara, M. M., & Russel, J. L. 1990, AJ, 99, 2082
Kambas, A., Davies, J. I., Smith, R. M., Bianchi, S., & Haynes, J. A. 2000, AJ, 120, 1316
Lanzetta, K. M., Yahil, A., & Fernández-Soto, A. 1996, Nature, 381, 759
Lupton, R. 2005, http://www.sdss.org/dr5/algorithms/sdssUBVRITransform.html
Mastropietro, C., Moore, B., Mayer, L., Debattista, V. P., Piffaretti, R., & Stadel, J. 2005, MNRAS, 364, 607
McCarthy, I. G., Balogh, M. L., Babul, A., Poole, G. B., & Horner, D. J. 2004, ApJ, 613, 811
Mihos, J. C. 2004, in Cluster of Galaxies: Probe of Cosmological Structure and Galaxy Evolution, ed. J. S. Mulchaey, A. Dressler, & A. Oemler (Cambridge: Cambridge Univ. Press), 278
Mohr, J. J., Geller, M. J., Fabricant, D. G., Wegner, G., Thorstensen, J., & Richstone, D. O. 1996, ApJ, 470, 724
Moore, B., Lake, G., & Katz, N. 1998, ApJ, 495, 139
Navarro, J. F., & White, S. D. M. 1994, MNRAS, 267, 401
Neumann, D. M., Lumb, D. H., Pratt, G. W., & Briel, U. G. 2003, A&A, 400, 811
Phillipps, S., Driver, S. P., Couch, W. J., & Smith, R. M. 1998, ApJ, 498, L119
Poggianti, B. 2004, in Proc. Baryons in Dark Matter Halos, Novigrad Croatia, ed. R. Dettmar, U. Klein, & P. Salucci (Trieste: SISSA), 104.1
Quilis, V., Moore, B., & Bower, R. 2000, Science, 288, 1617
Rhee, G. F. R. N., & Latour, H. J. 1991, A&A, 243, 38
Roettiger, K., Burns, J. O., & Loken, C. 1996, ApJ, 473, 651
Salpeter, E. E. 1955, ApJ, 121, 161
Salvador-Sole, E., Gonzalez-Casado, G., & Solanes, J. M. 1993, ApJ, 410, 1
Sarazin, C. L., O'Connell, R. W., & McNamara, B. R. 1992, ApJ, 397, L31
Schechter, P. 1976, ApJ, 203, 297
Smith, R. J., et al. 2004, AJ, 128, 1558
Smith, R. M., Driver, S. P., & Phillipps, S. 1997, MNRAS, 287, 415
Stetson, P. B. 1987, PASP, 99, 191
Struble, M. F., & Rood, H. J. 1999, ApJS, 125, 35
Thompson, L. A., & Gregory, S. A. 1993, AJ, 106, 2197
Tremonti, C. A., et al. 2004, ApJ, 613, 898
Trentham, N., & Tully, R. B. 2002, MNRAS, 335, 712
Wegner, G., Colless, M., Saglia, R. P., McMahan, R. K., Davies, R. L., Burstein, D., & Baggley, G. 1999, MNRAS, 305, 259
White, S. D. M., Briel, U. G., & Henry, J. P. 1993, MNRAS, 261, L8
Xia, L., et al. 2002, PASP, 114, 1349
Yan, H., et al. 2000, PASP, 112, 691
Yang, Y., et al. 2004, ApJ, 600, 141
Yuan, Q., Zhou, X., & Jiang, J. 2003, ApJS, 149, 53
Yuan, Q., et al. 2001, AJ, 122, 1718
Yuan, Q., et al. 2005, AJ, 130, 2559
Zhang, L., et al. 2010, Res. Astron. Astrophys., 10, 1
Zhou, X., et al. 1999, PASP, 111, 909
Zhou, X., et al. 2001, Chin. J. Astron. Astrophys., 1, 372
Zhou, X., et al. 2003, A&A, 397, 361